Nanoscale

Dynamic Article Links

Cite this: *Nanoscale*, 2011, **3**, 1316

www.rsc.org/nanoscale

REVIEW

Electrostatics at the nanoscale

David A. Walker,[a] Bartlomiej Kowalczyk,[ab] Monica Olvera de la Cruz[abc] and Bartosz A. Grzybowski*[ab]

Received 20th September 2010, Accepted 17th November 2010
DOI: 10.1039/c0nr00698j

Electrostatic forces are amongst the most versatile interactions to mediate the assembly of nanostructured materials. Depending on experimental conditions, these forces can be long- or short-ranged, can be either attractive or repulsive, and their directionality can be controlled by the shapes of the charged nano-objects. This Review is intended to serve as a primer for experimentalists curious about the fundamentals of nanoscale electrostatics and for theorists wishing to learn about recent experimental advances in the field. Accordingly, the first portion introduces the theoretical models of electrostatic double layers and derives electrostatic interaction potentials applicable to particles of different sizes and/or shapes and under different experimental conditions. This discussion is followed by the review of the key experimental systems in which electrostatic interactions are operative. Examples include electroactive and "switchable" nanoparticles, mixtures of charged nanoparticles, nanoparticle chains, sheets, coatings, crystals, and crystals-within-crystals. Applications of these and other structures in chemical sensing and amplification are also illustrated.

1. Introduction

Over the past several decades, chemists and materials scientists have developed numerous ways to synthesize nanoparticles (NPs) with increasingly well controlled[1–11] shapes, sizes, and polydispersities from a wide variety of materials, including metals,[1–4] polymers,[5,6] semiconductors,[7,8] oxides,[9,10] and other inorganic salts.[11,12] In addition to characterizing[1,13–15] the optical,[16–21] electronic,[19,22] mechanical,[23–31] and catalytic[23–27] properties of the individual NPs in solution, much effort has been devoted to implement methods to assemble these particles into larger ordered[28–33] or disordered[34–37] superstructures. These assembly strategies rely on the presence of many different types of interparticle interactions, including van der Waals (vdW),[37–40] magnetic,[41–44] electrostatic,[28,30,32,41–45] molecular dipole,[46,47] hydrogen bonding,[48–57] and covalent crosslinking.[58] The strength, range and directionality of these interactions can be controlled by the material properties of the NPs' cores,[37–40,59–62] the ligands on the particles' surface,[31,35,36,46] the solute surrounding the NPs,[28,30,47,63] or by external stimuli such as light,[35,47,64–67] pH,[46,68,69] temperature,[70–72] or applied field/potential.[73] While

[a]*Department of Chemical and Biological Engineering, Northwestern University, 2145 Sheridan Road, Evanston, Illinois, 60208, USA. E-mail: grzybor@norhwestern.edu*
[b]*Department of Chemistry, Northwestern University, 2145 Sheridan Road, Evanston, Illinois, 60208, USA*
[c]*Department of Materials Science and Engineering, Northwestern University, 2145 Sheridan Road, Evanston, Illinois, 60208, USA*

David A. Walker

David A. Walker graduated summa cum laude in chemical engineering from the University of South Florida with his B.S.Ch.E and M.S.Ch.E. jointly in 2008. He is currently a Ph.D. student in the Chemical and Biological Engineering department at Northwestern University and advised by Bartosz A. Grzybowski. His current work focuses on nano-scale electrostatics, and specifically how the shape of 'nano-ions' can be used to control self-assembly.

Bartlomiej Kowalczyk

Bartlomiej Kowalczyk obtained his M.Sc. and Ph.D. in chemistry from Warsaw University, Poland in 2000 and 2004, respectively. In 2006 he joined the lab of Bartosz A. Grzybowski at Northwestern University where he is now a Senior Research Associate. His current research is in the field of nanomaterials and using electrostatic self-assembly for the development of new nanoparticle based surface coatings.

many of these forces are strictly attractive or operate at a single characteristic length scale, electrostatic interactions between NPs can be either attractive or repulsive, and their magnitudes and range can be controlled by adjusting the charge on the NP surfaces, dielectric constant of the surrounding solvent or the NP core, or by the concentration of ions present in solution.

The fact that electrostatic interactions are so readily "adjustable" has motivated their use in numerous NP systems (see Fig. 1). One area of interest is the interactions between charged NPs and biological macromolecules (see Fig. 2). For example, charged particles interacting with proteins can change the electrostatic environment of the latter and thus affect the pK_a's of the acidic/basic amino acids. This, in turn, can cause denaturation of the protein,[74–76] an increase[77–79] or decrease[74,80–84] in protein activity, a change in the specificity of the active site,[82] or a shift in the active site's redox potential.[85–88] Many of these changes can be controlled by the nanoparticle "chaperone" itself – for instance, the shift in redox potential depends on the diameter of the NP.[87,88] Proteins are not the only biological molecules studied in conjunction with NPs. Another vibrant area of research focuses on the interactions between nanoparticles and (charged) DNA strands. The conformation of DNA tethered onto nanoparticles has been studied in the absence of complementary strands,[89] with single-stranded DNA used as a stabilizing ligand in salt solutions. Introducing complementary DNA strands induces NP assembly,[90–93] and mixtures of DNA-decorated NPs have been shown to self-assemble into linear chains,[94] ribbons,[94] and rings.[95] The principle of DNA-mediated NP self-assembly has provided the basis for high-precision assays recognizing multiple DNA targets[90,92] with sensitivity down to zeptomols.[96]

Electrostatic interactions between and assembly of charged NPs have been studied for a wide variety of particle shapes, including uniformly sized spheres,[28] cubes,[97] tetrahedra,[33,98] rods,[99] triangles,[99] as well as mixtures containing spheres with different diameters[63] and also mixtures of two differently shaped NPs.[99] The electrostatic effects underlying these assemblies derive from charged or dipolar functionalities within the self-assembled monolayers[88,100–102] (SAMs) which coat the particles. For interacting spheres, electrostatic forces mediate the formation of disordered aggregates or crystalline structures whose internal ordering depends on the charges[32] and sizes of the particles,[63] as well as the screening length.[28,30,32] In all cases, the observed crystal structures correspond to a minimum-energy configuration of the NPs.[28,30,32,103] Of course, electrostatic assembly methods are not limited to spheres. For instance, when nanocubes have zero, two, four, or five of their six faces coated with ionic ligands, these faces on different cubes repel one another causing the particles to organize into, respectively, three dimensional crystals,[97,104] flat sheets, linear chains, or doublets.[97] Electrostatic forces can also mediate the assembly of nanoscopic plates into large crystalline superlatticies,[105] can control mutual positions of charged particles with precision down to a few nanometers,[99] or can determine interactions with larger systems including living cells (where charge on nanosized particles affects their toxicity[106–108] and/or cellular uptake[109–111]).

There are two key components that determine electrostatic interactions in nanoparticulate systems. First is the charged molecules tethered onto the particle surface. Usually, these molecules form self-assembled monolayers – of thiols, disulfides, or dithiolanes on Au,[112,113] Ag,[114–116] Cu,[117–120] Pt,[121] Pd,[121–124] or Ni[125–127] NPs; of silanes on silica,[128–131] alumina[128–131] or titania,[132,133] of phosphoric[134,135] or carboxylic[135–137] acids on iron oxides, *etc.* While the chemistry of SAMs and the use of specific charged groups (COO^-, SO_3^-, PO_3^-, $N(CH_3)_3^+$) have been

Monica Olvera de la Cruz

Monica Olvera de la Cruz obtained her Ph.D. in physics from Cambridge University. She is the Lawyer Taylor Professor of Materials Science and director of the Materials Research Center at Northwestern University. From 1995–97 she was a Staff Scientist for CEA in Saclay, France. Monica has developed insightful models to describe the thermodynamics, statistics, and dynamics of assemblies of macromolecules, including copolymers and polyelectrolytes. Her work generated a revised model of ionic-driven assembly. She is a National Security Science and Engineering Faculty fellow, a fellow of the American Physical Society, and a fellow of the American Academy of Arts and Sciences.

Bartosz A. Grzybowski

Bartosz A. Grzybowski graduated summa cum laude in chemistry from Yale University in 1995. He obtained his doctoral degree in physical chemistry from Harvard University in August 2000 (with G.M. Whitesides). He joined the faculty of Northwestern University in 2003 and is currently a Kenneth Burgess Professor of Physical Chemistry and Chemical Systems Engineering and also director of the Non-Equilibrium Energy Research Center (a DoE Energy Frontier Research Center). His scientific interests include self-assembly in non-equilibrium/dynamic systems, complex chemical networks, nanostructured materials, and nanobiology. Bartosz' accolades include Soft Matter Award from RSC, ACS Colloids Unilever Award, AIChE Nanoscale Forum Young Investigator Award. He is also a Pew Scholar in the Biomedical Sciences, an Alfred P. Sloan Fellow, and a Dreyfus Teacher-Scholar.

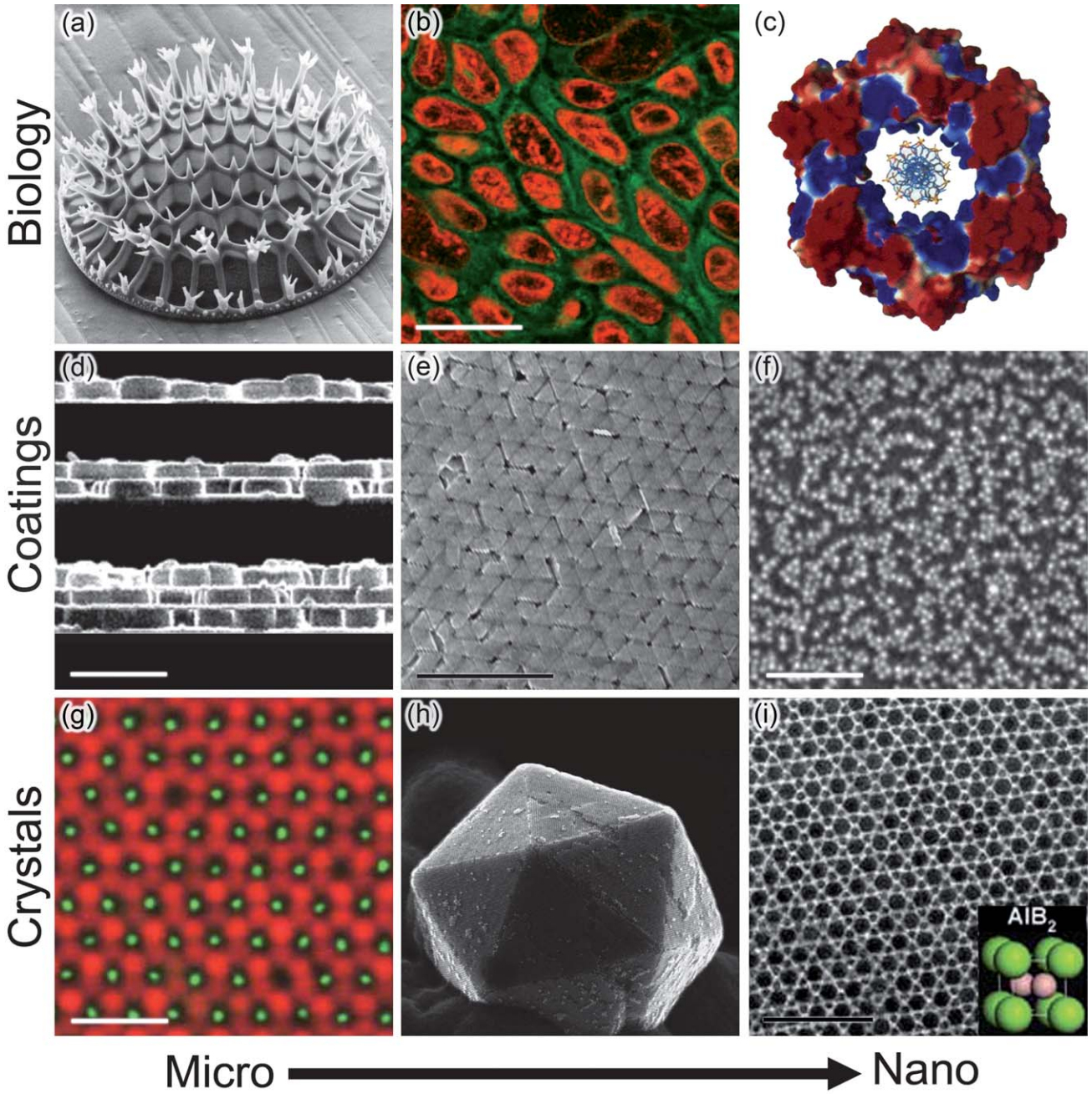

Fig. 1 Electrostatics in various systems/applications at micro- and nanoscales. **(a–c)** Biological examples include **(a)** biomineralization of charged inorganic/organic species (here, a fragment of a micro-organism called a diatom grown through the biomineralization of charged organosilicates; reprinted with permission from ref. 237), **(b)** cellular uptake of charged nanoparticles which is dependent on both charge polarity and magnitude (here, NPs located in the cytosol are functionalized with green fluorescent groups and NPs in the cell nuclei are functionalized with red fluorescent groups; scale bar is 20 μm; reprinted with permission from Elsevier, ref. 238) and **(c)** how surface potential within regions of a protein influences functionality. Shown here is the DNA binding β subunit from *E. coli* DNA polymerase III. Blue and red colors denote regions of positive and negative surface potential, respectively; the positive charge at the center of the protein facilitates DNA complexation. Reprinted with permission from AAAS, ref. 239. **(d–f)** Electrostatics is also a useful in assembling surface coatings. Examples include **(d)** the so-called layer-by-layer assembly (shown here are cross-sectional views of zeolite crystals assembled between polyelectrolyte layers on glass substrates; one, two and three zeolite layers are shown; scale bar is 1 μm; reprinted with permission from ref. 240; Copyright 2001 American Chemical Society), **(e)** the use of repulsive electrostatic interactions to drive crystallization of Raman-active, close-packed mono and multilayers of gold nanotriangles (scale bar is 1 μm; reprinted with permission from ref. 105; Copyright Wiley-VCH Verlag GmbH & Co. KGaA, 2010) and **(f)** the deposition of densely packed films incorporating negatively and positively charged NPs (scale bar is 100 nm; reprinted with permission from ref. 200; Copyright 2001 American Chemical Society). **(g–i)** Electrostatics also provides a versatile route to materials with crystalline ordering **(g)** Binary crystals of fluorescent charged microparticles (scale bar is 10 μm; Reprinted by permission from Macmillan Publishers Ltd: Nature Materials,[30] copyright 2003), **(h)** three dimensional crystals of oppositely-charged metal nanoparticles (reprinted with permission from ref. 169, Copyright Wiley-VCH Verlag GmbH & Co. KGaA, 2009) and **(i)** one of various binary nanoparticle superlattices (scale bar is 40 nm; Reprinted by permission from Macmillan Publishers Ltd: Nature Materials,[32] copyright 2006).

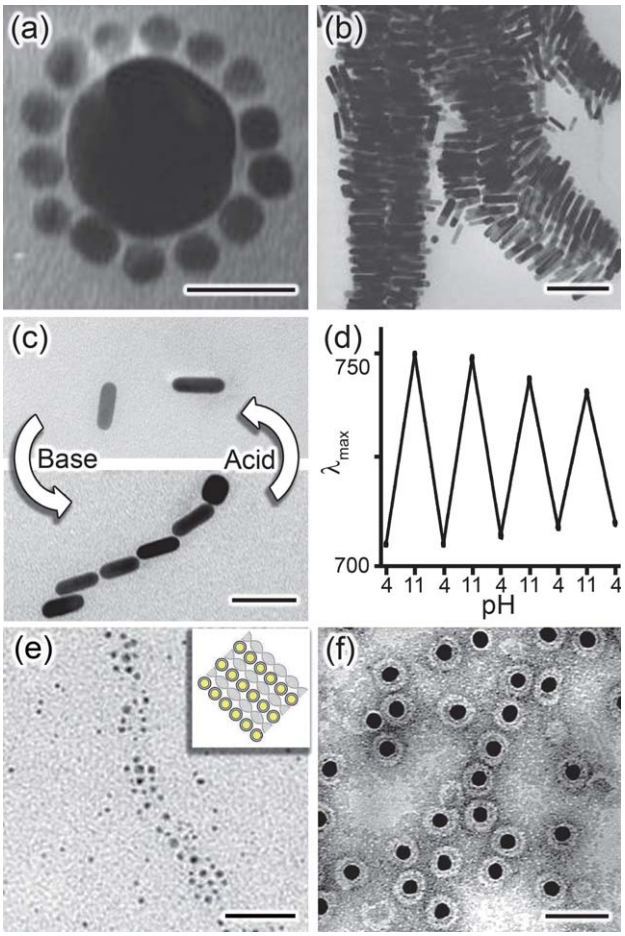

Fig. 2 Nanoparticle structures assembled using various charged biomolecules. Complimentary strands of DNA direct assembly of **(a)** spherical nanoparticles (reprinted with permission from ref. 241; Copyright 1998 American Chemical Society) or **(b)** rods (ref. 242; Reproduced by permission of The Royal Society of Chemistry). Scale bars are, respectively, 20 nm and 100 nm. **(c)** Reversible assembly of nanorods has also been achieved through the use of a conformational change in a pH responsive polypeptide, poly(L-glutamaic acid). Scale bar is 50 nm. **(d)** The assembly/disassembly cycles are monitored by the shifts in the position of the rods' longitudinal plasmon resonance. Reprinted with permission from ref. 46; Copyright 2008 IOP Publishing. **(e)** Charged strands of DNA have also been used to template the electrostatic assembly of nanoparticles into linear strands or bundles (as shown here). Scale bar is 25 nm. Reprinted by permission from Macmillan Publishers Ltd: Nature Materials,[94] copyright 2003. **(f)** Brome mosaic virus adsorbs onto NP surface *via* electrostatic attraction, and subsequently crystallizes into a capsid forming a 'virus like particle'. Scale bar is 50 nm. Reprinted with permission from ref. 243; Copyright 2006 American Chemical Society.

reviewed in detail elsewhere,[102,138–140] it should be mentioned that charge within the monolayer can be adjusted by the use of neutral "diluting" ligands—in this way, the so-called mixed SAMs (mSAMs) can be prepared with their net surface-charge density, σ, controlled by the fraction of charged molecules (for recent reviews of mSAMs, the reader is directed to[141,142]). In some interesting mSAM systems, the charged and uncharged thiols phase-separate to give "striped" nanoparticles—such inhomogeneous charge distributions lead to unusual forms of interparticle potentials (see ref. 143 and references therein).

The second way to control electrostatic effects in NP systems is through the electrostatic double layer (EDL) surrounding the particles. The EDL is comprised of solvent molecules and ions that are attracted to the charged surface, generally resulting in a locally increased concentration of counterions and decreased concentration of coions relative to their bulk-solution values. Importantly, the thickness of the EDL determines the range of electrostatic interactions in solution. The increased counterion and decreased coion concentration surrounding the particle causes the potential around the particle to decay exponentially with a characteristic length scale κ^{-1} (the Debye screening length). As more ions are added to the solution surrounding the NP, the value of κ^{-1} decreases so that the NPs need to be closer to one another in order to interact electrostatically.

Several theoretical models describing the EDL have been developed over the last 150 years, with their focus mainly on describing the interactions in colloidal systems. In an early model, Helmholtz[144] described the EDL as a monolayer of counterions on a charged surface. Later, Gouy[145,146] and Chapman[147] treated the EDL as a diffuse charged layer near a charged surface – this approach led to the so-called Poisson–Boltzmann equation, which we discuss in detail later in this Review. These fundamental continuum models have been refined to include the effects of counterion size, changes in the dielectric constant, and image charges; they have also been simplified into more analytically tractable forms that can be used to describe interactions between particles of various shapes, sizes, and compositions.

We will begin this Review by a detailed discussion of models describing the EDL. Since our focus is on nanoscopic systems, we will pay special attention to the fact that in this regime, the size of the counter or coions can be within an order of magnitude of the charged nano-object itself. A question that naturally arises is then whether the ions can be treated by the continuum formalism of partial differential equations (in particular, Poisson–Boltzmann) or does the description of the EDL need to account for the ions' discreet nature. Once we address these issues, we will then turn our attention to the theoretical description of the boundary between the nano-object and its ionic atmosphere. With these preliminaries, we will be in position to develop interaction potentials acting between charged objects of different shapes and sizes and will be able to rationalize electrostatic phenomena behind the experimental, nanoscale systems discussed in Section 4. Although this Review will certainly not be a complete survey of nanoscale electrostatics, we hope it will provide a comprehensive background and methodology to allow the readers to derive basic formulas describing their own systems of charged nano-objects.

2. Models of the electrostatic double layer

Generally, models of the EDL aim at determining the spatial concentration profiles/distributions of ions surrounding a charged object. These distributions can be determined by a number of different routes, including Monte Carlo (MC) or molecular dynamics (MD) simulations, integral equations and statistical mechanical models, or continuum descriptions of the local ion concentrations. What is important to remember is that each type of calculation has its advantages and limitations. The

MD/MC simulations and statistical models can be easily formulated to account for large numbers of interionic interactions, but they are limited by computational resources and can treat only relatively small systems. Continuum descriptions can be analyzed either analytically or numerically, but they discount the finite-size nature of the ions and many of the intermolecular interactions that appear in other models.

2.1 Molecular-level descriptions of the electrostatic double layer

At the molecular level, the distribution of ions within the EDL can be studied by either MD or MC methods with ion–ion interactions taken into account explicitly. Most commonly, either the so-called restricted primitive model (RPM) or the mean spherical approximation (MSA), are used. In RPM, the charged species (the NP and the ions surrounding it) are treated as hard-sphere objects that interact with one another *via* long-ranged interactions (*i.e.*, full Coulombic interactions) through a "continuum" solvent characterized by a uniform dielectric constant. The MSA retains the formulation of hard-sphere interactions between charged species from the RPM, but simplifies the long range interactions by linearizing the electrostatics. An offshoot of the MSA model is the MSA-HNC model (MSA with hypernetted-chain) which retains the hard-sphere interactions, improves the accuracy of the long range interactions by including non-linear electrostatics, and also accounts for short range interactions (*i.e.*, van der Waals forces). It should be remembered that the MSA linearization of the electrostatic interactions is a simplification that underestimates the interactions between highly charged particles and can give unphysical values for the ion distribution functions around a NP; hence the MSA-HNC is preferable under these circumstances.

The potential generated by an isolated charged particle at location $\mathbf{r}_i$ is $\varphi_i(\mathbf{r}) = \dfrac{z_i e}{4\pi\varepsilon_0\varepsilon|\mathbf{r}-\mathbf{r}_i|}$ and the electrostatic potential energy required to bring an additional charged particle, labeled j and of charge $z_j e$, from infinitely far away to a position $\mathbf{r}_j$ is given by

$$U_{ij}^{qq} = z_j e\big(\varphi_i(\mathbf{r}_j) - \varphi_i(\infty)\big) = \frac{z_i z_j e^2}{4\pi\varepsilon_0\varepsilon|\mathbf{r}_i - \mathbf{r}_j|} \tag{1}$$

where the potential of the charge on particle j is raised from zero to φ_j. When a system of charged particles and ions is considered, eqn (1) is written as a summation over all possible pairs. Since the potential's r^{-1} decay is long-ranged, simulations of the EDL around NPs must include a large volume of solvent, be periodic, or use an approximation for the potential far away from the charged surface. The hard-sphere interactions between ions, NPs and solvent molecules are defined by:

$$U_{ij}^{hs} = \begin{cases} \infty & |\mathbf{r}_i - \mathbf{r}_j| < a_i + a_j \\ 0 & |\mathbf{r}_i - \mathbf{r}_j| \geq a_i + a_j \end{cases} \tag{2}$$

which prevents particles from overlapping. While this expression can be used easily in MC simulations, the step change in potential causes an infinite force when particles overlap and thus cannot be easily implemented in MD simulations. To circumvent this challenge, the first line of eqn (2) is often approximated by a continuous function that rapidly diverges to ∞ as $|\mathbf{r}_i - \mathbf{r}_j|$ approaches $a_i + a_j$ so that no infinite forces can occur. The energy of the system may then be computed from the sum:

$$U = \frac{1}{2}\sum_i \sum_{j\neq i}\left(U_{ij}^{hs} + U_{ij}^{qq}\right) \tag{3}$$

where the infinite self-energy terms, U_{ii}^{qq} and U_{ii}^{hs}, are excluded from the summation and the leading factor of 1/2 prevents double counting of the electrostatic interactions.

Of course, charge-charge interactions are not the only electrostatic interactions that can affect NPs. The restricted primitive and MSA models neglect contributions due to induced electrical polarization of the NPs, ions and solvent, and also any permanent dipoles that may reside on the molecules comprising the solvent, both of which can significantly affect the distribution of ions around a NP. One way to account for polarization is to assign each NP, ion, and solvent molecule a dipole moment $\mathbf{p}$, that may be permanent (as in water), or induced (for example, by the electric field generated by the NP and EDL). The energetic contribution of these dipoles may be included by introducing the terms:

$$\begin{aligned} U_{li}^{pq} &= \frac{q_i \mathbf{p}_l \cdot (\mathbf{r}_i - \mathbf{r}_l)}{4\pi\varepsilon_0\varepsilon|\mathbf{r}_i - \mathbf{r}_l|^3} \\ U_{lk}^{pp} &= \frac{1}{4\pi\varepsilon_0\varepsilon}\left(\frac{\mathbf{p}_l \cdot \mathbf{p}_k}{|\mathbf{r}_l - \mathbf{r}_k|^3} - 3\frac{(\mathbf{p}_l \cdot (\mathbf{r}_l - \mathbf{r}_k))(\mathbf{p}_k \cdot (\mathbf{r}_l - \mathbf{r}_k))}{|\mathbf{r}_l - \mathbf{r}_k|^5}\right) \end{aligned} \tag{4}$$

where U_{li}^{pq} is the energetic contribution for charge–dipole interactions between charges i and dipoles l, U_{lk}^{pp} is the dipole–dipole term for dipoles l and k, and $\mathbf{p}_l$ is the dipole moment. Both U_{li}^{pq} and U_{lk}^{pp} must be summed over all unique interactions to find their total contribution to the electrostatic potential energy of the system.

The above expressions are only strictly valid in the case of a uniform dielectric constant. This assumption, however, is virtually never valid in systems of charged nanoparticles, where the dielectric constant of NP cores ranges from $\varepsilon \approx \infty$ (metallic NPs) to $\varepsilon \sim 2$ to 4 (polymeric NPs) while the surrounding solvents have dielectric constants ranging from $\varepsilon = 80.1$ (water) to $\varepsilon \sim 2$ (alkanes).[148] Therefore, the electrostatic interactions around the NP surface are effectively weighted by a mean dielectric constant. In the limit of strongly charged NP surfaces this dielectric renormalization can cause large charge accumulation of counterions in the EDL which further decrease the dielectric constant around the NP with respect to the value of the solvent at infinite distance.

If the dielectric constant varies, the potential must satisfy Poisson's equation of the form $\nabla\cdot(\varepsilon(\mathbf{r})\nabla\varphi(\mathbf{r})) = -\rho(\mathbf{r})/\varepsilon_0$ which relates the potential to the charge density, ρ, and dielectric constant, ε. Several methods have been developed to mathematically account for the variations in dielectric constant, as shown in Fig. 3, including the point-inducible dipole and local dielectric constant models for the entire system,[149] and application of the method of images for systems with isolated regions of non-uniform dielectric constant.[150] Finally, we note the most accurate simulations of EDL also take into account van der Waals dispersion forces and also magnetic dipole moments, both of which can also be expressed as sums of pairwise interactions.

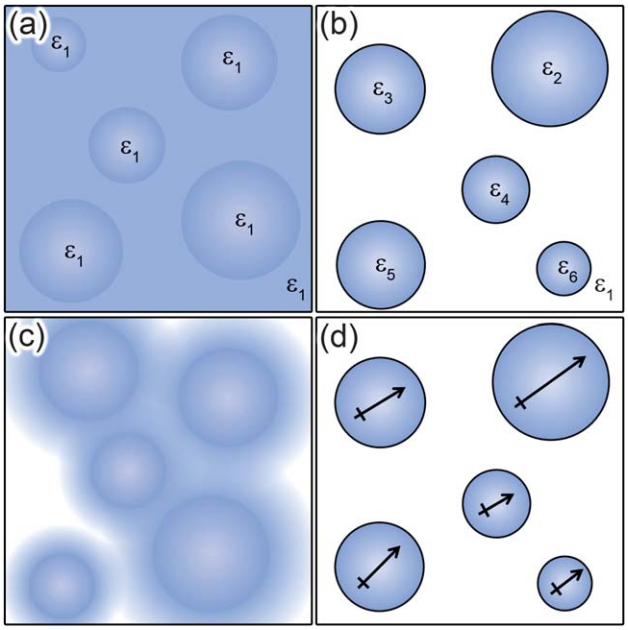

Fig. 3 Illustrations of various models used in defining the dielectric constant. The dielectric environment can be **(a)** constant across the entire region of interest (including inside any particles), **(b)** constant within defined local regions, **(c)** a continuous moving average across a region defined by external parameters (*e.g.*, local particle concentration), or **(d)** approximated by a series of well defined point dipoles.

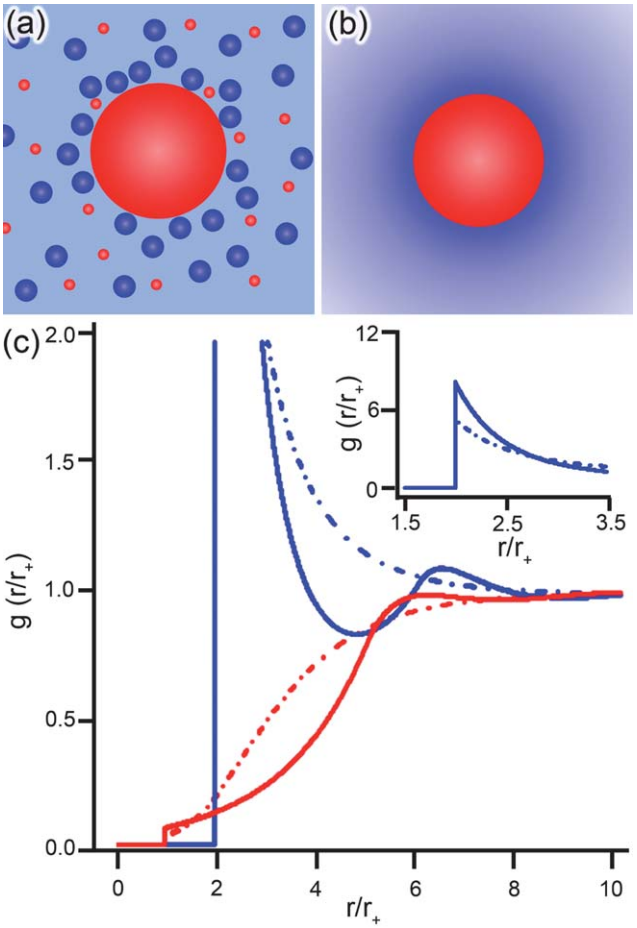

Fig. 4 Schematic representations of a positively charged NP (red) surrounded by charged counter/coions (blue/red) from two different theoretical perspectives. **(a)** The primitive model, PM, and mean spherical approximation, MSA, treat the NP and surrounding ions as hard spheres with the solvent as a continuum. **(b)** The PB models simplify the theoretical description by treating both solvent and ions as continuous distributions. **(c)** The radial distribution functions, g, of anions (blue, of radius $r_- = 0.425$ nm) and cations (red, of radius $r_+ = 0.2125$ nm) around a positive NP ($r_{NP} = 1.5$ nm, $q = 36$) as functions of the distance from the particle surface normalized with respect to the cation radius, r/r_+. The MSA/HNC model (solid lines, corresponds to diagram in (a)) shows an "oscillatory" behavior while the non-linear PB model with size-asymmetric ions (dashed lines, corresponds to diagram in (b)) predicts a monotonic behavior. Inset shows region not in view of the main graph.

What are the key results of the EDL simulations? In most cases, these methods yield distributions of counterions around charged objects similar to those predicted by continuum models (to be discussed in the next Section). Of course, there are notable exceptions which arise when the NP is either highly charged (when $\sigma > e/\ell_B^2$, where ℓ_B is the Bjerrum length discussed in Section 2.2; this corresponds to $\sigma > 0.33$ C m^{-2} for monovalent ions in water at 25 °C), for which MC simulations predict clustering or layering of the surrounding counterions,[151] or when the asymmetry in the size of the ions present in the EDL is significant enough that correlation functions describing the distributions of counterions and coions exhibit characteristic oscillations.[151–153] Such oscillations are illustrated in Fig. 4c, which has the MSA-HNC[154,155] radial ionic concentrations for both coions (red lines) and counterions (blue lines) around a nanoparticle. For comparison, the monotonic dependencies from a simple continuum model are also shown – while this continuum model can account for size asymmetry of co/counterions, it fails to describe properly the forces between the ions.

We note that for an infinitely dilute system of charged nanoparticles it has been shown that the ionic size asymmetry in monovalent electrolytes can promote an unequal charge neutralization (*i.e.*, ions of various sizes have different 'efficiencies' at screening charge) resulting in either charge inversion or charge amplification.[151,156,157] In such systems, charge inversion occurs when the native colloidal/nanoparticle charge is overcompensated at certain distances within the EDL by small counterions which adsorb on the NPs surface and screen charge more effectively than the larger counterions. Charge amplification occurs when the size-asymmetry of the surrounding ions causes more like-charged coions to be present around the particle or when a weakly charged nanoparticle adsorbs like-charged ions on its surface *via* other attractive interactions (*i.e.*, van der Waals interactions). Because continuum models based on PB equation do not account for many of these inter-ionic interactions, they rarely are able to predict the occurrence of these types of phenomena.[156–158] As a result, other theories which rely upon the PB equation also fail when there are strong electrostatic interactions between counterions residing close to a particle surface.[159–161] These inter-ionic correlations can be circumvented by using afore mentioned methods or by using density functional theories for nanoparticles.[162]

2.2 Continuum models of electrostatic interactions

The key difference between the continuum models and the discrete models discussed above is that instead of each charged

molecule being addressed individually, only the average concentration of each species is determined at each point in the simulation. In order to apply the tools of thermodynamics, it is necessary to assume that the EDLs surrounding the NPs have equilibrated with any externally applied fields and are in their thermodynamically favored state. This means that the electrochemical potential of each species present in the system must be constant throughout this system—this simple fact provides the necessary foundation from which analytical models for the EDL may be developed.

Since the energy of the system is a sum of electrostatic and non-electrostatic contributions (*e.g.*, hard sphere, van der Waals interactions, and dispersion forces due to the solvent), the changes of chemical potential from a reference state may be written as

$$\Delta\mu_e^k = \Delta\mu_c^k + \Delta\mu_{es}^k \tag{5}$$

where the superscript k denotes a particular species, μ_e denotes the electrochemical potential, μ_c denotes the chemical potential, μ_{es} the electrostatic potential, and the reference state is the electrolyte solution infinitely far from the NP. The chemical potential may be further broken down into (i) an ideal component, where $\Delta\mu_{c,\text{ideal}}^k = k_BT\ln(n_k(\mathbf{r})/n_k(\infty))$ represents the change in chemical potential due to concentrating or diluting the number density, n_k, relative to its concentration infinitely far from the particle, $n_k(\infty)$, and (ii) a correction that accounts for intermolecular forces, $\Delta\mu_{c,\text{real}}^k$. Similarly, the electrostatic potential for a point charge may be written as $\Delta\mu_{es}^k = z_ke(\varphi(\mathbf{r}) - \varphi(\infty))$[163] which accounts for the energy required to raise a particle with charge ez_k from potential $\varphi(\infty)$ to $\varphi(\mathbf{r})$ (e is the charge on an electron, z_k is the number of charges on the particle). Substituting these relationships into eqn (5), we then obtain:

$$\Delta\mu_e^k = k_BT\ln(n_k(\mathbf{r})/n_k(\infty)) + z_ke(\varphi(\mathbf{r}) - \varphi(\infty)) + \Delta\mu_{c,\text{real}}^k \tag{6}$$

From this expression, it is possible to determine the system-wide distribution of each ion by setting $\Delta\mu_e^k = 0$, which means that the electrochemical potential for each species is constant throughout the system (*i.e.*, the ions near the NP surface are in equilibrium with the bulk ions in the electrolyte) and applying the commonly used approximation that $\varphi(\infty) = 0$; this procedure gives:

$$n_k(\mathbf{r}) = n_k(\infty)\exp\left(-\frac{ez_k\varphi}{k_BT}\right)\exp\left(-\frac{\Delta\mu_{c,\text{real}}^k}{k_BT}\right) \tag{7}$$

Multiplying n_k by the charge per ion, ez_k, gives charge density, ρ, that can be substituted into the Poisson–Boltzmann equation, $\nabla\cdot(\varepsilon\nabla\varphi) = -\rho/\varepsilon_0$, to give:

$$\nabla\cdot(\varepsilon\nabla\varphi) = -\frac{e}{\varepsilon_0}\sum_k\left[z_kn_k(\infty)\exp\left(-\frac{ez_k\varphi}{k_BT}\right)\exp\left(-\frac{\Delta\mu_{c,\text{real}}^k}{k_BT}\right)\right] \tag{8}$$

Various sets of assumptions about the ion-ion and ion-particle interactions can be input into eqn (8), which serves as a basis for the most commonly used EDL theories that are derived from the PB equation. When the ions in the system are treated as ideal point charges, ε is constant in each phase (for instance, a NP core has $\varepsilon(\mathbf{r}) = \varepsilon_1$, the ligands in the SAM have $\varepsilon(\mathbf{r}) = \varepsilon_2$, and the solvent has $\varepsilon(\mathbf{r}) = \varepsilon_3$ – each area is a separate phase in terms of how the PB equation is applied) and the electrolyte is "symmetric" (that is, $z_{(+)} = -z_{(-)} = z$ and $n_{(+)}(\infty) = n_{(-)}(\infty) = n_\infty$), two important values can be introduced, the dimensionless potential, $\psi = ze\varphi/k_BT$, and the Debye screening length, $\kappa^{-1} = (k_BT\varepsilon_0\varepsilon/2e^2z^2n_\infty)^{1/2}$, so that:

$$\nabla^2\psi = \frac{2e^2z^2n_\infty}{k_BT\varepsilon_0\varepsilon}\sinh(\psi) = \kappa^2\sinh(\psi) \tag{9}$$

which is the most common formulation of the Poisson Boltzmann equation. Due to the nonlinearity introduced by the sinh term, it is difficult to integrate this equation analytically, and, unlike the MD and MC models above, the potentials from multiple charged NPs cannot be superimposed which means that the PB equation must be solved for every change of systemic variables. These difficulties, however, can be circumvented by using a linearized form of eqn (8):

$$\begin{aligned}\nabla^2\psi &= \frac{-e^2}{k_BT\varepsilon_0\varepsilon}\left[\sum_k z_kn_k - \sum_k z_k^2n_k\psi + \ldots\right]\\ &\approx \frac{e^2\sum_k z_k^2n_k}{k_BT\varepsilon_0\varepsilon}\psi = \kappa^2\psi\end{aligned} \tag{10}$$

where the first term in the brackets is zero due to the electroneutrality of the solvent, and the higher order terms of the Taylor expansion are ignored. This expansion is valid for $\psi < 1$, or $\varphi \leq 25$ mV at room temperature, and defines κ based on the ionic strength of the electrolyte solution. The major benefits of this linearization are that the equation can be integrated analytically and that its solutions can be superimposed allowing interaction potentials to be derived for many combinations of differently shaped nano-objects.

On the other hand, it should be emphasized that linearized PB equation cannot be used to model strongly charged systems, mainly because in such cases the ions around the NP cannot be treated as non-interacting and their correlations should be taken into account (see Section 2.1). The key quantity to be considered is then so-called Bjerrum length, $\ell_B = e^2/4\pi\varepsilon_o\varepsilon_rk_BT$, which is the distance at which the electrostatic potential energy of two elementary charges e in a solvent with a relative dielectric constant ε_r is comparable to the thermal energy k_BT. The corollary is that if two oppositely charged ions are within a distance l_B, they pair-up to decrease the electrostatic energy at the expense of entropy (thermal energy) they would gain if they were dissociated. Due to the high concentration of ions around a strongly charged nano-object, the local dielectric constant is low and the Bjerrum length can be over 1 nm indicating that the ions have a tendency to "pair up" and cannot be treated as independent.

Many extensions and corrections to the PB equation have been developed to estimate various effects that produce increasingly complex equations and generally provide a better fit to experimental data. For example, if hard-sphere interactions are considered between the electrolyte and the NPs, then the first layer of ions interacting with a charged surface cannot be adsorbed directly onto the surface and, instead, they are separated from the surface by one ionic radii. When all ions have the same size, this is represented by the so-called Stern model:[164,165]

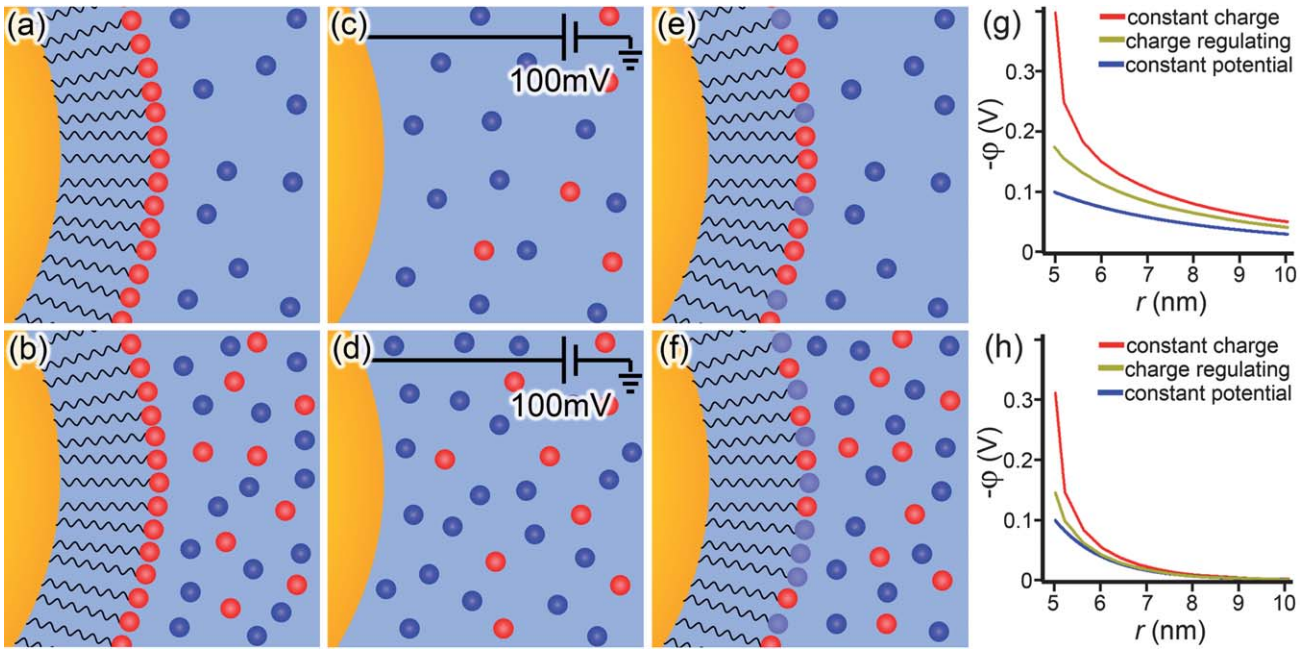

Fig. 5 Illustration of the three types of boundary conditions applied to PB model of a spherical NP. The constant-charge boundary condition in **(a,b)** keeps the charged density on the NP surface constant, regardless of (a) low or (b) high concentration of ions surrounding the particle. The constant-potential boundary in **(c,d)** fixes the surface potential of the NP and is, strictly speaking, appropriate only for "bare" nano-objects serving as electrodes. Finally, the charge-regulating boundary condition in **(e,f)** is much more dynamic in that neither the surface charge density nor the surface potential are kept constant, but rather remain functions of the ion concentration surrounding the particle by coupling a mass balance equation (which describes the number of ions on the NP surface which are disassociated and have a net charge) with the PB equation. Plots of each boundary condition under **(g)** low and **(h)** high ion concentration show the differences in potential profiles around the NP ($r_{NP} = 5$ nm).

$$\nabla^2\psi = \begin{cases} 0 & 0 < \mathbf{r}' < a_{ion} \\ \kappa^2 \sinh(\psi) & a_{ion} < \mathbf{r}' \end{cases} \tag{11}$$

where $\mathbf{r}'$ is measured from the surface outward rather than from the center of a particle, and ψ is subject to a matching condition at $\mathbf{r}' = a_{ion}$ and $\mathbf{r}' = 0$ at the charged surface. This theory was extended by Valleau and Torrie to include two different sized ions, of radii a_1 and a_2, where $a_1 < a_2$. In this model, two Helmholtz layers are formed – one for each type of ion (see monotonic functions in Fig. 4c). The potential in this system then decays as:

$$\nabla^2\varphi = \begin{cases} 0 & 0 < x < a_1 \\ -\dfrac{ez_1 n_1(\infty)}{\varepsilon_0 \varepsilon} \exp\left(-\dfrac{ez_1\varphi}{k_B T}\right) & a_1 < x < a_2 \\ -\dfrac{e}{\varepsilon_0 \varepsilon} \displaystyle\sum_{k=1}^{2} z_k n_k(\infty) \exp\left(-\dfrac{ez_k\varphi}{k_B T}\right) & a_2 < x \end{cases} \tag{12}$$

These more detailed descriptions of the double layers around charged particles can predict phenomena such as overcharging of nanoparticles[151] and are more appropriate for highly charged surfaces. They also provide a good first approximation for the potential when the size asymmetry between counter- and coions is large without requiring the additional computations *via* molecular-level models.

2.3 Boundary conditions

As for every partial differential equation, the PB equation requires the boundary conditions to be specified. The most important of these conditions—one reflecting the nature of the charged nano-object—is at the particle/solution interface and accounts for the way in which the particle acquires charge in solution through, typically, the dissociation of counterions. As in all other electrostatic systems, the potential at the NP/solvent interface must be continuous, $\varphi^{in} = \varphi^{out}$, and Gauss's law must be satisfied, $(\varepsilon^{in}\nabla\varphi^{in} - \varepsilon^{out}\nabla\varphi^{out})\cdot\mathbf{n} = \sigma/\varepsilon_0$, where $\mathbf{n}$ is the outward normal to the interface, and the superscripts *in* and *out* denote the particle and solvent, respectively. While the potential is calculated, and the dielectric constant specified, the surface charge density, σ, remains to be defined. In most systems of charged NPs, a dissociable group is exposed on the surface of a self-assembled monolayer, SAM, stabilizing the particle. The dissociation of ionizable groups in a SAM, $AB \rightleftarrows A^{\pm} + B^{\mp}$, is characterized by the equilibrium constant $K_d = 1/K_b = [A^{\pm}][B^{\mp}]/[AB]$, where K_d is the dissociation constant and K_b is the association/binding constant. If the molecules comprising the SAM were free in solution, the dissociation of each individual molecule would not affect other molecules. However, when the dissociable molecules are tethered onto a surface, the dissociation of each molecule causes a subsequent increase in the potential of the nearby molecules (if their cationic portions remain adsorbed; as in SAMs of alkane thiols terminated in $-N(CH_3)_3^+$), or a decrease in the potential (if the anionic portions of the molecules remain adsorbed; as in SAMs of alkane thiols terminated in $-COO^-$). This interplay between potential and association/dissociation of the ligands and ions from solution causes this form of boundary to be known commonly as a "charge-regulating" boundary condition.[166,167]

In order to calculate the value of σ from the equilibrium between neutral and dissociated molecules on the NPs, the number of molecules per unit area, Γ, is multiplied by the average number of charges per molecule, γ, so that $\sigma = \Gamma\gamma$. The value of Γ is constant for flat surfaces and is equal to the surface density of ligands in the SAM. For curved surfaces (*e.g.*, cylinders or spheres), however, Γ depends not only on the surface density but also on the radius of curvature and the length of the molecules forming the SAM (see Fig. 9a, and Section 4.1.2 for further discussion). For example, Γ on the outer surface of a 5 nm diameter particle coated with a 1 nm thick SAM decreases to ~51% of its flat surface value, while the same thickness SAM on a 100 nm diameter particle results in only a 4% decrease in Γ. The value of γ is determined by three factors (i) the value of K_d for the ions/ligands in solution, (ii) the concentration of ions in solution, and (iii) the potential at which the ligands are relative to the bulk of the solution. When the number of ions in solution is much greater than the number of ligands on the surface of the NPs (as is the typical case), then the concentration of ions infinitely far away is effectively constant, so the concentration of ions at the surface can be predicted using eqn (7) as:

$$[X]_s = [X]_\infty \exp\left(-\frac{z_x e\varphi(s)}{k_B T}\right) \tag{13}$$

where X represents an ion that binds to the SAM, the subscripts s and ∞ denote, respectively, the surface of the SAM and the location infinitely far away, and z_x is the valence of X. Substituting this equation into the expression for chemical equilibrium, and assuming that the value of $[X]_\infty$ does not change due to adsorption leads to $\gamma = K_d\exp(z_x e\varphi(s)/k_B T)/[X]_\infty$ for electrolytes and adsorbed ligands that have the same valence. For systems where the ligands and counterions have different magnitudes of charge, each combination of ligands and counterions must be treated as a separate species. The calculation of γ then requires a mass balance to conserve the amount of adsorbed ligands in addition to equilibrium constants describing the dissociation of each species.[168]

While the charge regulating boundary provides the most detailed description of the interaction between the ligands and ions in solution, there are two other commonly used approximations that are more mathematically tractable. The first is the constant charge condition, which occurs when the ligands retain the same charge regardless of potential—that is, no counterions or coions bind to the ligands and K_d is, strictly speaking, infinite (or at least very large as for very strongly acidic groups such as SO_3^-). The other limiting case that is commonly analyzed is the constant potential boundary condition, in which the potential of the surface is kept constant regardless of the concentration of electrolyte in the system. This boundary condition is most appropriate for a system that is connected to a potential source (*i.e.*, a battery or an electrode)—for example unprotected NPs adsorbed onto an electrode. In terms of dispersed NPs, an approximation to this condition would require an infinite density of charged groups, with a K_d approaching zero, but a finite non-zero value of $K_d\Gamma$.[169] The three types of boundary conditions are illustrated in Fig. 5.

3. Energetics of the electrostatic interactions at the nanoscale

3.1 Energies of interaction between charged nanoparticles

Knowing the structure of the EDL and the appropriate boundary conditions sets the stage for calculating the free energies of interactions between charged nano-objects. In general, three distinct contributions to the free energy must be considered, (i) the potential energy due to electrostatic interactions, (ii) the entropic contribution from concentration of ions near the charged particle, and (iii) the chemical potential energy changes due to ion adsorption/desorption. The electrostatic potential energy is given in its typical form of:

$$U_{es} = \frac{\varepsilon_0}{2}\int_V (\mathbf{E}\cdot\mathbf{D})dV = \frac{1}{2}\int_A \sigma\varphi_0 dA + \frac{1}{2}\int_V \rho\varphi dV \tag{14}$$

where the first integral is the energy as a function of the electric field, **E**, and the electric displacement, **D**. The second expression is a continuous version of eqn (3), with the first term accounting for the energy of the charged surfaces, and the second term accounting for the energy of the double layer surrounding these surfaces.

The entropic contribution in dilute solution is given by:[170]

$$\Delta S = -k_B\int_V\left\{\sum_i n_i\ln\left(\frac{n_i}{n_{io}}\right) + n_s\ln\left(\frac{1-\sum_i 1-x_i}{1-\sum_i 1-x_{io}}\right)\right\}dV$$

$$\approx -k_B\int_V\left\{\sum_{i\neq s} n_i\ln\left(\frac{n_i}{n_{io}}\right) - n_i + n_{io}\right\}dV \tag{15}$$

where i enumerates all species in the solution, including the solvent (denoted by a subscript s), subscript "o" denotes the location infinitely far from the charged surface, n is the concentration, and x is the mole fraction. Substituting in eqn (7) for ideal solutions allows the introduction of the potential into this relationship as:

$$\Delta S = k_B\int_V\left\{\sum_{i\neq s} n_{io}[z_i\exp(-z_i\psi) + \exp(-z_i\psi) - 1]\right\}dV \tag{16}$$

Recognizing that the first term in the summation is similar to the charge density in the double layer, and applying an integral transformation, the entropic contribution can be written as:

$$-T\Delta S = \varepsilon\varepsilon_0\int_V\left(\varphi\nabla^2\varphi - \int_0^\varphi \nabla^2\varphi' d\varphi'\right)dV \tag{17}$$

The free energy of the system (note that the Helmholtz and Gibbs free energies are identical if the ion distribution does not induce a change in solution volume) is then derived by the application of Green's formula and the addition of a progress variable (for details see Ref. 170):

$$G_{es} = U_{es} - T\Delta S = \int_A\int_0^\sigma \varphi_{surf}(\sigma')d\sigma' dA \tag{18}$$

where φ_{surf} is the potential at the charged surface which, for charge regulating NPs, varies nonlinearly with σ.

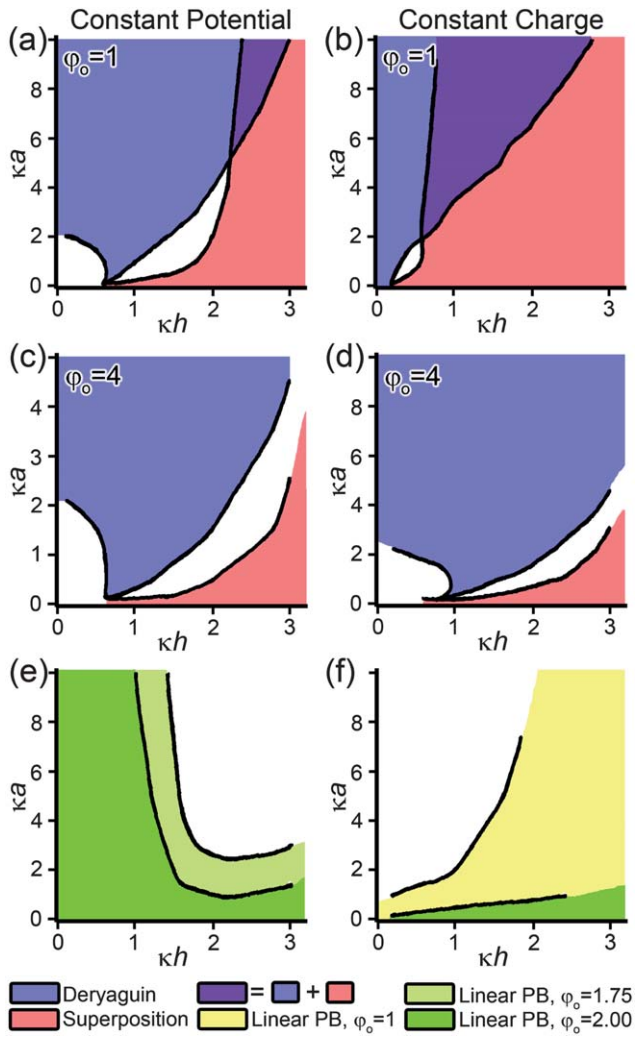

Fig. 6 Phase diagrams depicting where either the Derjaguin or linear superposition approximations yields a force between two particles which deviates by less than 10% from the non-linear PB equation. Diagrams depict **(a)** constant potential or **(b)** constant charge boundary conditions where the dimensionless surface potential is $\varphi_o = 1$ and **(c)** constant potential or **(d)** constant charge boundary conditions where $\varphi_o = 4$. **(e, f)** Direct comparison between linearized and non-linear PB equation under either **(e)** constant potential or **(f)** constant charge boundary conditions at various values of dimensionless surface potential. The shaded regions represent conditions where the force between two nanoparticles calculated by linearized PB equation deviates by less than 10% from non-linear PB equation for surface potentials equal to or less then the indicated value. Plots are adapted with permission from Elsevier, ref. 176.

We note that this potential only accounts for the electrostatic portion of the free energy, and neglects any change in free energy due to the adsorption of ions at the charged interface. To include this energetic contribution after the formation of the monolayer, we use eqn (5), with $\Delta\mu_c^k$ equal to the energy released when an ion dissociates or associates and $\Delta\mu_{es}^k = z_k e\varphi_{surf}$; at equilibrium, $\Delta\mu_c^k = -z_k e\varphi_{surf}$ for each individual ion pair. In order to integrate this over the area, the surface charge density is used instead of $z_k e$, giving:[167,170]

$$G_{chem} = -\int_A \sigma\varphi_{surf}\, dA \tag{19}$$

The overall change in free energy is then given by the sum:

$$G = G_{es} + G_{chem} = -\int_A \int_0^{\varphi_{surf}} \sigma(\varphi')\, d\varphi'\, dA \tag{20}$$

This result can also be derived using charging processes, or interaction forces.

The derived energy can be used to calculate the free energy of interaction between charged NPs. If the isolated particles are taken as a reference state, the free energy of interaction between N particles is given as:

$$\Delta G = G_{sys} - NG_{iso} \tag{21}$$

where G_{sys} is the free energy of the assembly, and G_{iso} is the free energy of each particle when it is infinitely far from the assembly. Note that these energy calculations do not assume any particular form for the potential and can thus be used for any models of the EDL presented above. Eqn (14), (16), and (19) may be integrated for a single equilibrium configuration with a defined potential and ion distribution in order to calculate the free energy of the system, making them well suited for models that are inherently numerical – for example MD, MC, and the PB equation. At the same time, the calculation of the free energy from a charging process (eqn (14), (17) and (20)) can be easily applied to systems where the potential and charge density can be derived analytically – as in the PB equation between parallel plates and the linearized form of the PB equation.

3.2 Approximate expressions for energetic interactions

While eqn (18) will always give the free energy of the system, it is often not feasible to perform the integration over all surfaces/particles, especially in large systems (*e.g.*, NP aggregates). It then becomes convenient—and, indeed, necessary—to introduce appropriate approximations, of which the so-called Derjaguin and linear-superposition (LSA) approximations are the most useful and popular.

In the Derjaguin approximation,[171–173] the interaction between non-planar particles is simplified by assuming that the interaction energy (or force) per unit area is the same as for infinite parallel plates. Specifically, the interacting curved particles are approximated as sets of infinitesimal parallel plates separated by a distance h'. The interaction energy is then calculated by multiplying the interaction energy per unit area for parallel plates, $u_{pp}(h')$, by the area of the curved surfaces at a given separation, $A(h')$, then integrating over all distances h':

$$U = \int_h^\infty u_{pp}(h')A(h')dh' \tag{22}$$

When applied to two interacting spheres,[173] with radii a_1 and a_2, the Derjaguin approximation gives the interaction potential

$$U = \frac{2\pi a_1 a_2}{a_1 + a_2}\int_h^\infty u_{pp}(h')dh' \tag{23}$$

Table 1 Electrostatic interaction energies for various particle shapes and configurations derived by applying the Derjaguin approximation to the solution of flat plates with either constant charge or constant potential boundary conditions.[225,244] In these equations, h is the minimum separation distance between the particles' surfaces, and a is the characteristic radius specific to the problem (*i.e.*, for the sphere/sphere interaction, a_1 and a_2 correspond to, respectively, the radius of particle 1 and that of particle 2; for the cylinder/sphere interaction, a_c and a_s correspond to the characteristic radius of the cylinder and of the sphere, respectively)

Geometry	Potential	Boundary Condition	Range
Sphere/Sphere $\sigma_o = \sigma_{o,1} = \sigma_{o,2}$ $a = a_1 = a_2$	$U_{es} = -2\pi\varepsilon\varepsilon_o a\varphi_o^2 \ln(1 - \exp(-\kappa h))$	Constant Charge	$\kappa a \gg 1$ $\varphi_o \leq 25$ mV
Sphere/Sphere $\varphi_o = \varphi_{o,1} = \varphi_{o,2}$ $a = a_1 = a_2$	$U_{es} = 2\pi\varepsilon\varepsilon_o a\varphi_o^2 \ln(1 + \exp(-\kappa h))$	Constant Potential	$\kappa a \gg 1$ $\varphi_o \leq 25$ mV
Sphere/Sphere $a = a_1 = a_2$	$U_{es} = 2\pi\varepsilon\varepsilon_o a\varphi_o^2 \exp(-\kappa h)$	Constant Charge or Constant Potential	$\kappa a < 5$ $\varphi_o \leq 25$ mV
Plate/Plate $\sigma_o = \sigma_{o,1} = \sigma_{o,2}$	$U_{es} = \frac{\sigma_o^2}{\varepsilon\varepsilon_o\kappa}\left[\frac{1+\exp(-\kappa h)}{\sinh(\kappa h)}\right]$	Constant Charge	$\varphi_o \leq 25$ mV
Plate/Plate $\varphi_o = \varphi_{o,1} = \varphi_{o,2}$	$U_{es} = \varepsilon\varepsilon_o\kappa\varphi_o^2[1 - \tanh(\kappa h/2)]$	Constant Potential	$\varphi_o \leq 25$ mV
Plate/Plate $\varphi_{o,1} \neq \varphi_{o,2}$	$U_{es} = 1/_2\varepsilon\varepsilon_o\kappa\left[\begin{array}{c}\left(\varphi_{o,1}^2 + \varphi_{o,2}^2\right)(1 - \coth(\kappa h)) \\ + 2\varphi_{o,1}\varphi_{o,2}\mathrm{cosech}(\kappa h)\end{array}\right]$	Constant Potential	$\varphi_o \leq 25$ mV
Sphere/Sphere $a_1 \neq a_2$	$U_{es} = 2\pi\frac{a_1 a_2}{a_1 + a_2}\int_h^\infty U_{es,plates}\,dx$	Given by $U_{es,plates}$	Any from $U_{es,plates}$ $\kappa a \gg 1$ $a > h$
Cylinder/Cylinder (Side-to-Side)	$U_{es} = \sqrt{\frac{2a_1 a_2}{a_1 + a_2}}\left(\int_h^\infty \frac{U_{es,plates}}{\sqrt{x-h}}dx\right) \times \text{Length}$	Given by $U_{es,plates}$	Any from $U_{es,plates}$ $\kappa a \gg 1$ $a > h$
Cylinder/Cylinder (Crossed)	$U_{es} = 2\pi\sqrt{a_1 a_2}\int_h^\infty U_{es,plates}\,dx$	Given by $U_{es,plates}$	Any from $U_{es,plates}$ $\kappa a \gg 1$ $a > h$
Cylinder/Sphere	$U_{es} = \frac{2\pi a_s\sqrt{a_c}}{\sqrt{a_s + a_c}}\int_h^\infty U_{es,plates}\,dx$	Given by $U_{es,plates}$	Any from $U_{es,plates}$ $\kappa a \gg 1$ $a > h$
Plate/Sphere	$U_{es} = 2\pi a\int_h^\infty U_{es,plates}\,dx$	Given by $U_{es,plates}$	Any from $U_{es,plates}$ $\kappa a \gg 1$ $a > h$

in which the exact functional form of u_{pp} depends on the specific boundary conditions at the particles' surfaces (see Table 1 for functionals for constant charge and constant potential boundary conditions).

In LSA, it is assumed that the potential of the entire system may be written as a sum of the potentials of isolated particles:

$$\varphi(\mathbf{r}) = \sum_i \varphi_i^{iso}(\mathbf{r} - \mathbf{r}_i) \tag{24}$$

where each individual particle is located at $\mathbf{r_i}$ and has a potential φ_i^{iso} when it is infinitely far from other objects.

These approximations have been compared to exact integrations for both the linearized[174,175] and nonlinear[176] PB equations for interacting spheres in terms of dimensionless diameters, κa, and κh, where a is the NP radius and h is the distance between the charged surfaces of the NPs. As shown in Fig. 6, the Derjaguin approximation for the force between two spheres is generally within 10% of the exact nonlinear PB solution for small separations and $\kappa a > 2$, while it entails more than 10% error when used for smaller κa values. To understand these comparisons in terms of actual physical dimensions and concentrations, we note that if two 5 nm diameter spheres are interacting, the Derjaguin approximation would be valid if the concentration of a symmetric monovalent electrolyte surrounding them were ~60 mM or greater.

The Derjaguin approximation is very useful because the nonlinear PB equation can be solved in a closed form between

Table 2 Van der Waals interaction energies for various particle shapes and configurations derived from Hamaker summations between two particles (*i.e.*, pairwise summation of the intermolecular forces[225,245–247]). In these equations, A is the Hamaker constant which is specific to the composition of each particle and the surrounding solvent, h is the minimum separation distance between the particles surfaces, and a is the characteristic radius specific to the problem

Geometry	Potential	Range
Sphere/Sphere	$U_{vdw} = \frac{-\mathrm{A}}{6h}\left(\frac{a_1 a_2}{a_1 + a_2}\right)$	$a_1,a_2 \gg h$
Sphere/Sphere	$U_{vdw} = \frac{-16\mathrm{A}a_1^3 a_2^3}{9h^6}$	$a_1,a_2 \ll h$
Plate/Plate (semi-infinite)	$U_{vdw} = \frac{-\mathrm{A}}{12\pi h^2} \times \mathrm{Area}$	
Plate/Plate (finite thickness, d)	$U_{vdw} = \frac{-\mathrm{A}}{12\pi}\left[1/h^2 - 2/(d+h)^2 + 1/(d+2h)^2\right] \times \mathrm{Area}$	
Cylinder/Cylinder (Side-to-Side)	$U_{vdw} = \frac{-\mathrm{A}}{12\sqrt{2}h^{3/2}}\left(\frac{a_1 a_2}{a_1 + a_2}\right)^{1/2} \times \mathrm{Length}$	$a_1,a_2 \gg h$
Cylider/Cylinder (Side-to-Side)	$U_{vdw} \propto \frac{-1}{h^5} \times \mathrm{Length}$	$a_1,a_2 \ll h$
Cylinder/Cylinder (Crossed)	$U_{vdw} = \frac{-\mathrm{A}\sqrt{a_1 a_2}}{6h}$	$a_1,a_2 \gg h$
Plate/Sphere	$U_{vdw} = \frac{-\mathrm{A}a}{6h}\left(1 + \frac{h}{2a+h} + \frac{h}{a}\ln\left(\frac{h}{2a+h}\right)\right)$	$a \gg h$
Plate/Sphere	$U_{vdw} \propto \frac{-1}{h^3}$	$a \ll h$

parallel plates. This allows for the force or interaction energy between two nano-objects to be expressed in a closed form as well – that is, a reasonably accurate estimation of the forces/energies can be made without using more complicated numerical techniques. On the other hand, when the particles are far apart, the LSA provides a better estimate than the Derjaguin formalism. This is so because, as the distance from a nano-object increases, the values of φ and $\partial\varphi/\partial r$ both decrease to zero. Thus, if one were to calculate the energetic change of a system of NPs using these approximations, the LSA should be used for the particles being far apart, while the Derjaguin approximation should be used for more closely spaced particles.

The linearized PB equation is, as expected, more accurate for lower potentials in both the constant-charge and constant-potential situations. Interestingly, this approximation is better for small separations in the constant potential case, and for large separations in the constant charge case; consequently, one must use caution when applying it to any charge-regulating systems.

While the numerical integration of both forms of the PB equation for interacting spheres is no longer a technical challenge, it is often convenient to use one of many analytical approximations for the interaction between different objects. For instance, the free energy of two interacting spheres that are separated by a distance $r > \kappa^{-1}$ can be written as:

$$U_{es} = \frac{Q_1^{\infty} Q_2^{\infty}}{4\pi\varepsilon_0\varepsilon(1+\kappa a_1)(1+\kappa a_2)} \frac{\exp[-\kappa(r-a_1-a_2)]}{r} \quad (25)$$

where Q_i^{∞} is the renormalized charge on the sphere i at infinite separation, and the functional form of $U(r) = \mathrm{b}\exp(-cr)/r$ is commonly known as a Yukawa or screened Coulombic potential. When the surface potential of the particles is low, $\varphi < k_B T/e$, the system is in the linear regime, so the potential outside a sphere ($r > a$) can be approximated as:

$$\varphi_i(r) \approx \frac{Q_i^{\infty}}{4\pi\varepsilon_0\varepsilon(1+\kappa a_i)} \frac{\exp[-\kappa(r-a)]}{r} \quad (26)$$

In the low potential limit, the renormalized charge is proportional to the surface charge density, $Q_i^{\infty} = 4\pi a_i^2 \sigma_i^{\infty}$. At large surface potentials ($\varphi \approx 4k_B T/e$), the renormalized charge saturates, and can be estimated using eqn (26) as

$Q_i^{\infty} = 4\pi\varepsilon_0\varepsilon a_i(1 + \kappa a_i)(4k_BT/e)$. This has been further extended in the case of the linearized PB equation in both series and closed forms for spherical particles with different diameters and all possible combinations of constant charge, charge regulating, and constant potential boundary conditions.[177] Similar approximations have been derived for interactions between spheres, plates and rods in multiple configurations as shown in Table 1, were a's denote radii of the interacting particles, and h is the separation between their surfaces.

In real NP systems, these potentials are often considered in conjunction with attractive vdW interactions between the NPs (Table 2 lists potentials for some typical geometries). In this table the characteristic radius of the problem is a, the separation between the particle surfaces is h, and A is the Hamaker coefficient specific to the material/solvent system. This juxtaposition is the basis of the so called Derjaguin-Landau-Verwey-Overbeek, DLVO, theory,[170,171,178–180] which yields total interaction potentials such as those illustrated in Fig. 7 for like-charged spherical particles.

3.3 Limitations of pairwise continuum interactions

Although, as we have discussed, the Derjaguin approximation and LSA are good for many types of interparticle interactions, they become less accurate at small κa and κh, where the EDL thickness, particle size and particle separation are all of similar magnitude, which is especially relevant to charged nanoparticles. Also, as two particles approach one another, the EDLs around them merge causing the ions within the layers to redistribute around the entire particle as opposed to the local redistribution that occurs at large κa. When a third particle is introduced to the system, its interaction causes further adjustment of the EDL not only due to the distances between the individual particles (pairwise interactions), but also from contributions due to all three EDLs interacting (three-body interactions). In systems of like-charged particles, pairwise interactions (*i.e.*, particles 1 and 2, 2 and 3, and 1 and 3) are all repulsive, however, recent experimental[181–184] and theoretical[183,185–187] work has shown that three-body interactions between like charged particles can be attractive in systems where $\kappa a \sim 1$. Conceptually, the addition of a third charged particle screens the interaction between the other two, thus making the three-body contribution energetically favorable. Interestingly, both two- and three-body interactions in nonlinear PB systems can be well approximated by the so-called Yukawa potentials.[185] The two-body interactions are represented as $U = A_2 \exp(-\kappa r)/r$, while the three- body interactions scale as $U = -A_3 \exp(-\gamma L)/L$ where $L = r_{12} + r_{23} + r_{13}$ is the total distance between particle centers and the parameters A_2, A_3 and γ depend on the charge and the screening length of the system. While the pairwise and three-body interactions have the same profile, the total distance between particle centers in the three-body interactions will typically be longer than the pairwise interactions, so the energetic contribution of each three-body interaction will be less than each pairwise interaction; however, there are many more three-body interactions in close packed structures than two-body ones, so the overall energy of forming an extended structure can be favorable. It must be remembered though, that these undisputedly fascinating effects are still poorly understood and more fundamental work is needed before they can be used to explain formation of specific nanostructures.

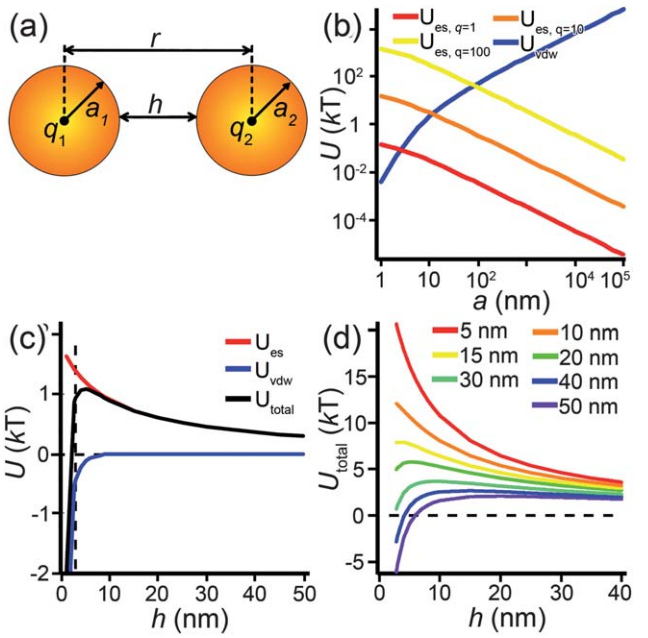

Fig. 7 **(a)** Scheme of interacting NPs of radius a_i and charge q_i, whose surfaces are separated by distance h. **(b)** Plots of the magnitudes of electrostatic, U_{es}, and van der Waals, U_{vdw}, energies for NPs of charge $q = 1e$, $10e$, and $100e$ as a function of NP radius, a, at a fixed separation of $h = 2.8$ nm (twice the thickness of a C_{12} SAM). **(c)** Electrostatic, van der Waals, and total energy profiles as a function of separation between two 10 nm NPs of charge $q = 5e$. Electrostatic forces are long-ranged compared to the van der Waals interactions that dominate at smaller separations (the separation distance due to the thickness of the SAMs is indicated by the vertical dashed line). The net energy barrier at a finite separation prevents particle aggregation. **(d)** U_{total} profiles for NPs of various radii. All electrostatic interactions shown here are for the case of unscreened NPs ([Ions] = 0, $\kappa^{-1} = \infty$) of charge $q = 15e$. In all plots, the van der Waals interactions are calculated for Au NPs with water as the solvent (Hamaker constant, $A = 9 \times 10^{-20}$J).

4. Nanoscale electrostatics in practice—key systems and experiments

Armed with the basic knowledge of the fundamentals of nanoscale electrostatics, we are now in position to review the recent studies involving charged nano-objects. We will begin by discussing the properties of individual charged nanoparticles, will then focus on the basic aspects of interparticle interactions, and will conclude with the discussion of large assemblies and materials comprised of charged NPs.

4.1 Individual charged particles

4.1.1 Structure of the charged self-assembled monolayers. Structure of the charged SAMs stabilizing nanosized objects has been the subject of several recent works. Of particular interest for our subsequent discussion are the results obtained by Vernizzi and Olvera de la Cruz,[188] who showed that charged ligands on particles form a more homogeneous SAMs than uncharged ones. This is illustrated in Fig. 8 which shows the results of a MC simulation based on a coarse grained model in which each ligand is represented as a string of N monomeric units. The difference in

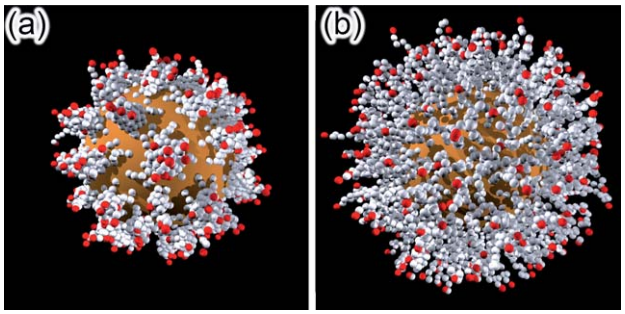

Fig. 8 Monte Carlo simulation of spherical nanopartciles functionalized with ligands having hydrophobic tails terminated in **(a)** uncharged and **(b)** charged groups. In SAMs presenting charged end-groups, the ligands are more strateched out and form a more homogeneous monolayer. In both cases, the simulation accounts for 392 ligands, 10 monomers each, bound to a 5 nm particle (as in, for example, 5 nm AuNPs covered with alkane thiolates).

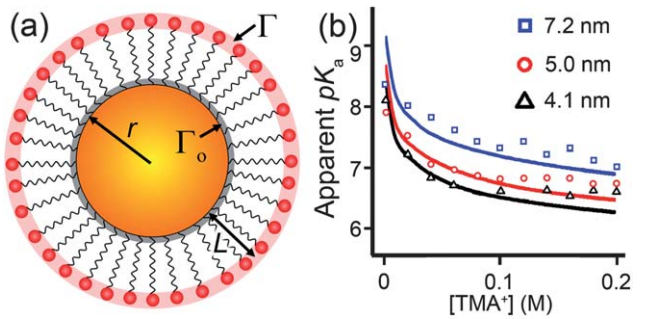

Fig. 9 **(a)** Scheme of a nanoparticle or radius r covered with a SAM of charged ligands (of thickness L). The density of charged end-groups at the outermost surface of the SAM is $\Gamma = \Gamma_o(r/r + L)^2$ where Γ_o is the density of binding sites for ligands on the NP (*e.g.*, $\Gamma_0 \approx 4.7$ nm^{-2} for alkane thiols on Au[190]). **(b)** The apparent pK_a of carboxylic acids bound to a NP surface is a function of the bulk ionic concentration of the surrounding solution, and also of the NP radius. Here, we see that a difference of ~3 nm in the NP core diameter leads to a change of ~1 pH unit in the pK_a. Markers correspond to experimental data, lines are theoretical fits.[248]

SAM structures is due to the interplay between hydrophobic and electrostatic forces, which can be quantified by a simple energy functional:

$$E_{int} = 4\varepsilon \sum_{i<j} \left[(\sigma/r_{ij})^{12} - (\sigma/r_{ij})^{6} \right] + k_B T \, l_B \sum_{i<j} \left[e^{-\kappa r_{ij}}/r_{ij} \right] + E_{hc} + E_{bond} \tag{27}$$

where the first term is a Lennard-Jones potential effectively describing hydrophobic attractions between monomers $i,j < N$, separated by distance r_{ij}, the second term is a screened Coulombic potential (a.k.a. Yukawa potential) accounting for the repulsions between the charged end groups (l_B is the Bjerrum length, k_B is the Boltzmann constant, κ is the inverse-screening length, T is the absolute temperature), E_{hc} is a hard-sphere potential preventing the ligands from overlapping, and E_{bond} accounts for limited stretchability of the "bonds" between the monomers (see Ref. 189). The various parameters of the model are calibrated against experimental studies described in Ref. 28.

When MC simulations are performed according to the Metropolis algorithm and with simulated annealing cooling schedule, the typical equilibrium configurations are such as those in Fig. 8. For the uncharged end-groups (Fig. 8a), the energy of the system is dominated by the hydrophobic interactions between the chains, which tend to bundle together and form "patches," whose number depends strongly on the grafting density of the ligands as well as their chain length. On the other hand, when the end groups are charged (Fig. 8b), the electrostatic repulsions dominate – in particular, for relatively short chain lengths (6–12 monomeric units, corresponding to typical alkane thiolates used to stabilize nanoparticles), these repulsions prevent bundling and the ligands stretch out into the surrounding solvent maximizing the average distances between the charged groups and effectively rendering the SAMs more homogeneous. This relative homogeneity partly justifies the use of continuum models in which the charge density on the surface of NPs is, for a given particle size/curvature, treated as constant.

4.1.2 Effects of nanoparticle curvature on ligand's pK_a. While the density of ligand grafting is an inherent property of the NP core/ligand interface (*e.g.*, $\Gamma_0 \approx 4.7$ nm^{-2} for thiolate ligands on gold[190]), the density of the charged-end groups at the surface of the SAM depends on the curvature of the particle (*e.g.*, for SAM thickness L and finite particle radius r, charge density of the end-groups is $\Gamma = \Gamma_o(r/r + L)^2$, see Fig. 9a). Since this dependence is most pronounced for small particle radii, it is reasonable to assume that in this regime the effects of interactions between charged groups are most pronounced. One manifestation of such interactions should be the dependence of the pK_a on R – indeed, our group has recently studied this effect both experimentally (*via* potentiometric titration method[191]) and theoretically in collections of AuNPs of different sizes and covered with mercaptoundecanoic acid (MUA) ligands. The markers in Fig. 9b plot the apparent pK_a's for different values of R and also as a function of salt concentration. As seen, the larger the particle, the higher the pK_a – this observation can be rationalized by the fact that when the particle size increases, the charged headgroups are, on average, closer together and their deprotonation requires more basic conditions (since it is energetically more costly to abstract protons from a surface that has a higher density of charged groups than from a more curved surface on which Γ is smaller). The decrease of pK_a with increasing salt concentration can also be rationalized by qualitative energetic arguments – when, for a given R, there is more salt, it screens the electrostatic repulsions between the charged groups so that it is easier to deprotonate them compared to the situation when these groups "feel" one another (electrostatic energy is more unfavorable then).

Of course, these intuitive arguments cannot substitute for a "real" theory. A notable – though relatively complex – theoretical treatment has been developed by Szleifer *et al.* and accounts for the free energies of acidic ligands as well as the surrounding counterions. We emphasize that the use of free energies rather than potential energies is necessary to model the equilibrium constants and, consequently, the pK_a dependencies. In this approach,[192–194] the free energy functional F, is written as

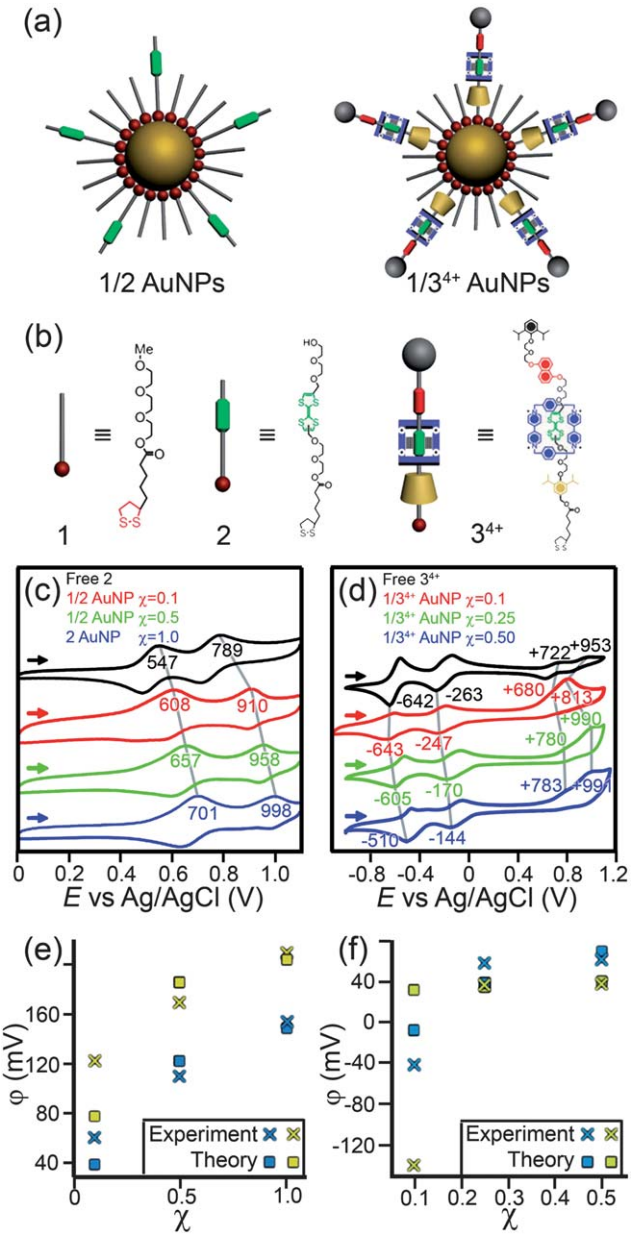

Fig. 10 **(a)** Scheme of AuNPs functionalized with electron-rich TTF stalks (*left*) and bistable [2]rotaxanes (*right*). **(b)** Structural formulae of the ligands. **(c,d)** Cyclic voltammograms of ligands **(c) 2** and **(d) 3**$^{4+}$ present free in solution and adsorbed on Au NPs at various surface concentrations, χ. **(e,f)** Experimental ($\times$) and calculated ($\square$) shifts in the redox potential, φ, of TTF in **(e) 1/2**-Au NPs and **(f) 1/3**$^{4+}$-Au NPs as a function of the surface coverage, χ. Blue and yellow traces correspond to the first and second oxidation potentials of TTF, respectively. Adapted with permission from ref. 168. Copyright 2010 American Chemical Society.

a sum of several contributions, $F = -TS_{mix} - TS_{conf} + E_{vdw} + E_{rep} + E_{elec} + F_{chem}$, where T is the temperature, S_{mix} is the mixing entropy of the mobile species (cations, anions, water, hydroxyl ions, and protons), S_{conf} is the conformational entropy of the grafted ligands, E_{vdw} is the energy of the attractive van der Waals interactions, E_{rep} accounts for the steric repulsive interactions between all the molecular species, E_{elec} is the total electrostatic energy, and F_{chem} represents the free energy associated with the acid–base chemical equilibrium, which is the free energy associated with the degree of protonation and deprotonation of the acid groups. While the mathematical details of this model are well beyond the scope current Review, it is worth noting that the model treats explicitly all possible conformations of the NP-grafted ligands and configurations of ions, and weights their energetic contributions according to the principles of statistical mechanics. This exhaustive treatment translates into a singular accuracy of this approach – the pK_a trends predicted by the model (see solid lines in Fig. 9b) are in close agreement with experimental data.

4.1.3 Redox properties of nanoparticle-immobilized organics. The finite size and curvature of the NPs can also affect the redox properties of electroactive ligands. We have recently demonstrated[168,195] that the attachment of redox active ligands or Stoddart-type rotaxanes to the NP surfaces affects their redox potentials. For example, oxidation potentials of dithiolane-terminated tetrathiafulvalene (TTF) "struts" (marked as **2** in Fig. 10b) were found to be higher after their NP immobilization than in solution, and depended on the surface concentrations, χ, adjusted by varying the ratio of **2** to the background ligand **1** in the mixed SAMs. The observed gradual increase of the oxidation potentials with increasing χ (Fig. 10c) can be attributed to the accumulation of positive charge on the surfaces of NPs. Oxidation of **2** on a NP increases the electric potential, making it more difficult to oxidize other TTF ligands on the same particle. Dithiolane-terminated bistable [2]rotaxane **3**$^{4+}$ showed an analogous behavior, with the reduction potentials of the cyclobisparaquat-*p*-phenylene (CBPQT^{4+}) "ring" shifted to more positive values (Fig. 10d). These shifts indicate that as the surface concentration of CBPQT^{4+} increases (and the positive charge accumulates), it becomes gradually easier to reduce these groups, and therefore to decrease the unfavorable electrostatic potential energy of the system.

In the context of our discussion of nanoscale electrostatics it is important to note that these results can be quantified by relating the shifts in redox potential, E, to the changes in the electrostatic potential around the particles, φ. Two observations are relevant here: (*i*) that the oxidation of ligands X adsorbed on NP surfaces causes φ around the particle to increase and (*ii*) that the more of the oxidized species are already present on the surface, the more difficult it is to oxidize more of these groups and introduce additional charge onto the particle (negative electrostatic cooperativity). Based on these premises, it can be expected that the oxidation potential of adsorbed X is related to φ: to the first approximation, one can write $E^x = E^0 + \varphi$, where E^x is the observed oxidation potential at the particle's surface (metal core plus SAM) and E^0 is the oxidation potential of molecule X in a dilute solution. In other words, the shift in the oxidation potential $E^x - E^0$ is equal to the electrostatic potential due to the immobilized ligands, φ. The value of the latter is found readily by solving the by-now familiar Poisson–Boltzmann equation, $\nabla^2\psi = \kappa^2\sinh(\psi)$, where κ^{-1} is the Debye screening length, and $\psi = e\phi/kT$ is the dimensionless potential. Importantly, the dependence of the potential on the surface concentration of the ligands, χ, and the curvature/radius of the nanoparticle, R, influences the solution to the problem *via* the boundary condition of the form $\left.\frac{\partial\phi}{\partial r}\right|_{r=R} = -\frac{\sigma(X,\chi)}{\varepsilon_0\varepsilon}$, where σ stands for the surface charge density on the NP. While other mathematical details can

be found in ref. 195 and 168, the key point is that this relatively straightforward model predicts accurately – to within less than 5% – the changes in redox potentials for NPs of different sizes and functionalized with various types of redox-active molecules including structurally complex pseudorotaxanes, bistable [2]rotaxanes (Fig. 10e,f), or catenanes. Lastly, the model is generic in the sense that it can be easily adapted to other types of charged switches.

4.1.4 Individual nanoparticles—coda. The take home message from this Section is that the finite size and/or the curvature of the NPs affect the particles' degree of ionization, net charge, or the redox properties. One of the most common mistakes in treating charged NPs is to assume that their properties are simply a sum of the properties of the individual charged ligands. This is certainly far from the physical reality and it must be remembered that a SAM constrained to the particles' nanoscopic surface is a conglomerate of groups for which electrostatic potentials are coupled to chemical equilibria (ion dissociation/association).

4.2 Aggregates of charged nanoparticles

Isolated charged nano-objects such as those described in previous Sections are an idealization and in real experiments the sample contains multiple particles. While the interactions between like-charged objects are typically strictly repulsive and incapable of bringing these particles together (but see Section 4.2.2 below), the mixtures of oppositely charged NPs appear naturally suited for the assembly of larger structures. We will first

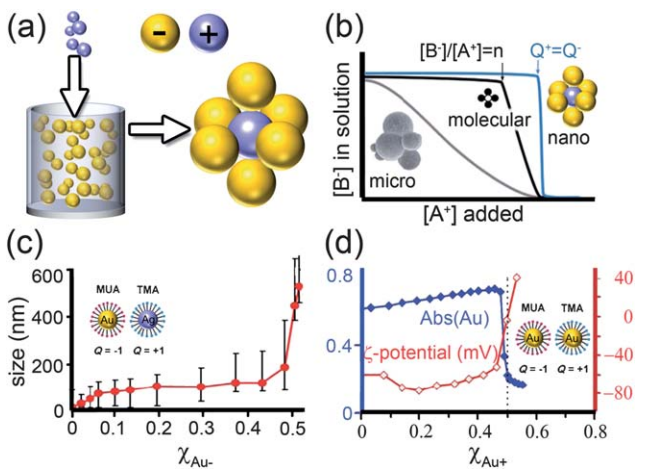

Fig. 11 **a)** Scheme of the titration experiment in which a solution of negatively charged NPs (*e.g.*, Au/SH-$(CH_2)_{11}$-COO^-, MUA; *yellow*) is titrated with a solution containing positively charged NPs (*e.g.*, Ag/SH-$(CH_2)_{11}$-$N(CH_3)_3^+$, TMA; *blue-gray*). When a small number of positively charged NPs are added to a large number of negatively charged NPs, they form clusters whose negative surface charge stabilizes them in solution. **b)** The titrated nanoparticles precipitate from solution sharply only upon reaching the point of whereby the charges on the NPs are balanced. In contrast, molecular ions precipitate at the product of solubility, whereas oppositely charged colloids precipitate continuously. **c)** Average size of aggregates measured by DLS during titration of 11 nm AuMUAs with 11 nm AgTMAs. **d)** Intensity of the Au SPR band at λ_{max} 520–550 nm (blue line) and the values of the ζ-potential (red line) for the titrations of oppositely charged, 5.5 nm AuNPs. Figure adapted with permission from ref. 190. Copyright 2006 American Chemical Society.

describe phenomena in which the charged NPs form either smaller and/or internally disordered aggregates—the assemblies and materials exhibiting long-range crystalline ordering will be described in Section 4.3.

4.2.1 Oppositely charged, spherical nanoparticles in solution. What happens when solutions containing objects bearing charges of opposite polarities are mixed (Fig. 11a)? It depends on the scale and is thought to be fundamentally different in the molecular and in the colloidal regimes. Whereas oppositely charged ions can remain stable in solution until reaching a certain threshold (determined by pertinent equilibrium constants, such as the solubility product, K_{sp}) at which they start to precipitate, oppositely charged microparticles precipitate continuously over a wide range of relative particle concentrations.[196–198] Recently, it was shown that charged nanoparticles exhibit neither of these behaviors and, instead, precipitate only at the point of NP electroneutrality—that is, when the charges on the NPs are compensated, $\sum Q_{NP(+)} + \sum Q_{NP(-)} = 0$ (see Fig. 11b).[190,199–202]

Naturally, as the titration progresses, the oppositely charged NPs aggregate—this is evidenced both by the dynamic light scattering, DLS, data in Fig. 11c as well as the red-shifting of the particles' SPR band (blue curve in Fig. 11d). Surprisingly, however, the surface potential of the forming aggregates remains constant (red curve in Fig. 11d) despite the fact that the added/"minority" NPs have charge opposite to that of the "majority" particles originally present in solution. Only when the solution is about to precipitate, the magnitude of the potential decreases rapidly and is zero at the precipitation point (Fig. 11d). These findings—supported by UV-Vis spectroscopic analyses[203] as well as theoretical considerations[199,201]—indicate that the NPs form aggregates whose outer shells contributing to surface potential are composed mostly of the "majority" particles (Fig. 11a). These shells render all aggregates like-charged and stabilize them in solution by mutual electrostatic repulsions. When the net charge on the NPs is close to neutral, there are not enough "excess" NPs to form like-charged shells, and precipitation ensues.

These results pose some interesting questions. Why, one might ask, are the NP clusters forming before the point of electroneutrality stable despite having net charge? And why, in the first place, is the sharp precipitation a nanoscale-specific phenomenon not seen with larger, microscopic particles?[196–198] To answer these questions, we observe that the solutions of NPs before precipitation point are stable not only kinetically for a given period of time, but also thermodynamically (in experiment, for months). This property implies that NP aggregation can be explained based on the energies of interparticle interactions.

To calculate electrostatic interparticle interactions, we can use the formalism developed in Sections 2 and 3 to first solve for the electrostatic potential, φ, and then derive the free energy of interaction *via* the thermodynamic integration method described in detail in ref. 177, 178. Since the potentials around charged NPs are usually less than ~50 mV, the linearized version of the Poisson–Boltzmann (PB) equation, $\nabla^2\varphi = \kappa^2\varphi$, can be used together with the "charge-regulating" boundary conditions we discussed in Section 2.3. For the case of an individual NP coated with N_T positively charged surface ligands, A^+, in a solution containing negatively charged counterions, B^-, the counterion dissociation equilibrium is determined by

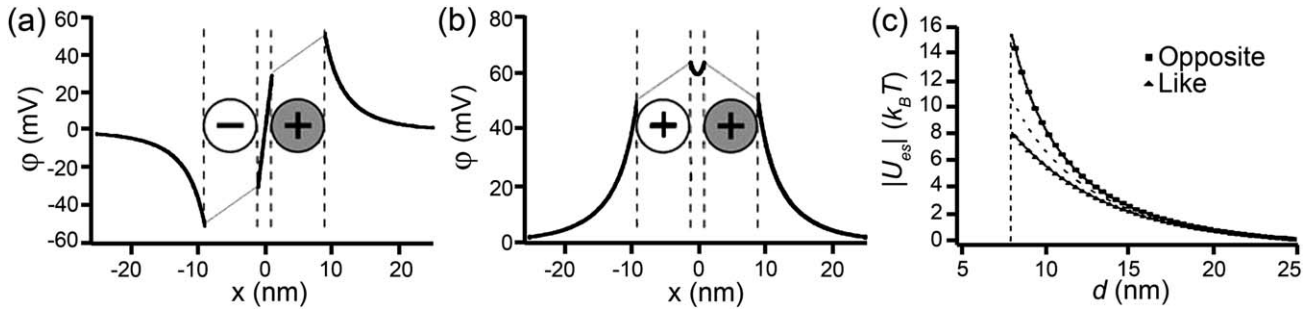

Fig. 12 **(a,b)** Electrostatic potential along the axis, x, connecting two **(a)** oppositely charged and **(b)** like charged NPs. Note that the potential is smaller between oppositely charged NPs, resulting in desorption of counterions and enhanced electrostatic attraction. The potential is larger between like-charged NPs, causing further adsorption of counterions and reduced electrostatic repulsion. **(c)** Magnitude of the electrostatic interaction energy, $|u_{es}|$, between two oppositely charged and two like-charged NPs as a function of the distance between their centers, d. The dashed line is the approximate form $u_{es}(d) = 4\pi\varepsilon_0\varepsilon\varphi_s^2R^2\exp[-\kappa(d - 2R_1)]/d$. Reprinted with permission from ref. 190. Copyright Wiley-VCH Verlag GmbH & Co. KGaA, 2007.

$N_{A+}\ C_{B-}/N_{AB} = K_+ \exp(e\varphi_s/k_BT)$, where N_{A+} and N_{AB} are, respectively, the numbers of counterion-free and counterion-bound surface ligands ($N_{A+} + N_{AB} = N_T$), C_{B-} is the concentration of counterions in solution, K_+ is the equilibrium constant in the absence of any external fields, and φ_s is the electrostatic potential at the NP's surface. From this relation, the surface charge density, σ, may be expressed as $\sigma = e\rho/[1 + (C_{B-}/K_+)\exp(e\varphi_s/k_BT)]$, where $\rho = N_T/4\pi R^2$ is the surface density of charged groups, and R is the NP radius. Assuming the dielectric constant of the NPs ($\varepsilon_p \approx 2$ for the SAM coating) is small compared to that of the solvent ($\varepsilon \approx 80$ for water), the surface charge is related to the potential at the NP surface by $\sigma = -\varepsilon_0\varepsilon\nabla\varphi\cdot\vec{n}$, where $\vec{n}$ is outward surface normal. Equating the two relations for σ provides the necessary boundary condition for a positively charged NP and allows us to solve for the equilibrium constant of the charged ligands; the case of a negatively charged particle may be derived in a similar fashion.

Once the equilibrium constant of the charged ligands is known on a single NP, the linearized PB equation must be solved numerically in conjunction with the linearized charge regulating boundary conditions[177] for the case of two interacting NPs. This process yields potential profiles which are used to calculate the interaction potentials in Fig. 12.

The striking feature of these dependencies is that the attractive energy between oppositely charged NPs at contact is nearly twice that of like-charged NPs at the same distance. This effect is due to the desorption of bound ions from the NPs' surfaces in the regions of reduced electrostatic potential (*cf.* the equilibrium relation above). Specifically, when oppositely charged NPs approach one another, the magnitude of the potential in the region between them decreases (Fig. 12a) causing counterions to desorb. This desorption, in turn, increases the local charge density and the electrostatic interaction energy. In contrast, the magnitude of the potential between proximal, like-charged NPs is enhanced (Fig. 12b), causing further adsorption of counterions, decrease in the local charge density, and reduction of the electrostatic interaction energy. The differences in the like-charged and oppositely charged interaction potentials are of central importance in rationalizing the core-shell NP clusters observed in experiments (*cf.* Fig. 11a)—colloquially put, the like-charge repulsions are more effectively screened than opposite-charge attractions, and so the like-charged NPs can form the "shells" stabilizing the NP aggregates forming before the point of electroneutrality is reached.

An interesting corollary of the NPs' singular precipitation behavior is the ability to control precisely the fractions of charged ligands on NP surfaces. Here, one begins by preparing "standard" NPs—typically, noble-metal nanoparticles of known size and fully covered with alkane thiols terminated in a charged functionality. Since the area of the surface occupied by each thiol is known (*e.g.*, 21.4 Å^2 for Au[204]) the charge of the "standard" is readily calculated. Then, to read the unknown charge on

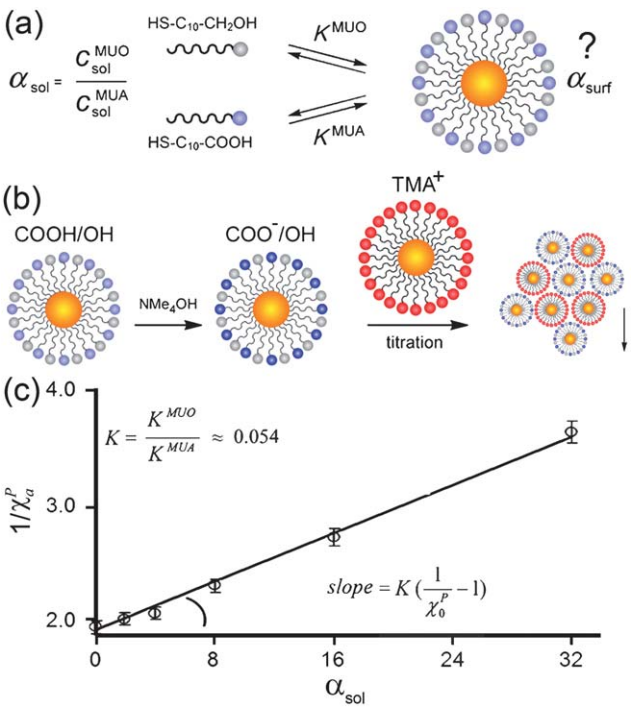

Fig. 13 **(a)** The proportions of the MUA and MUO thiols in solution (α_{sol}) and in the mixed SAM on the NPs (α_{surf}) are not equal. **(b)** To determine α_{surf} and the ratio of adsorption equilibrium constants, K, the MUA/MUO NPs are first deprotonated and then titrated with TMA NP "standards". **(c)** The value of K is calculated from the slope of the dependence of $1/\chi_\alpha^P$ on α_{sol}. Reprinted with permission from ref. 190. Copyright Wiley-VCH Verlag GmbH & Co. KGaA, 2007.

nano-objects of a different type, the solution of the "unknowns" is titrated with that of the "standards," and the precipitation point where $\sum Q_{NP(+)} + \sum Q_{NP(-)} = 0$ reports the charge on the former. The precision of this method is within ~3%, and we have found it particularly useful in determining charges of NPs covered with mixed self-assembled monolayers (*m*SAMs) composed of charged and uncharged thiols. Fig. 13 illustrates this method applied to NPs covered with a *m*SAM of 11-mercaptoundecanol ($HS(CH2)_{11}OH$; MUO) and 11-mercaptoundecanoic acid ($HS(CH_2)_{10}COOH$; MUA), in a molar ratio $\alpha_{surf} = c^{MUO}_{surf}/c^{MUA}_{surf} = x/y$. Naively, one might expect that *m*SAM of such composition, can be prepared by simply soaking non-functionalized, "bare" NPs in a solution containing x moles of MUO and y moles of MUA. In reality, the surface composition obtained in this way almost certainly will *not* be x:y, since the equilibrium constants for the adsorption of different thiols are different (Fig. 13a). Instead, a series of solutions of different proportions of the two thiols (say $\alpha_{sol} = 0,2,4,8,16, 32, \ldots$) are prepared and their pH adjusted to 11 to deprotonate all MUA's carboxylic groups. This solution is then titrated with like-sized NPs fully covered with positively charged TMA thiols and the positions of the precipitation points χ^Pas a function of α_{sol} are recorded. To determine equilibrium constants from these experiments, we note that the absorption equilibrium constant of each thiol onto AuNPs is given by $K^T = c^T_{Au}/c^T_{sol}c_{Au}$, where T = MUO or MUA, c^T_{Au} is the concentration of thiol adsorbed onto AuNPs, c^T_{sol} is the concentration of free thiol in solution, and c_{Au} is the concentration of free adsorption sites on the surface of AuNPs. Because the mole fraction of MUA thiol on the surface can be written as $\eta^{MUA} = 1/[1 + \alpha_{sol}(K^{MUO}/K^{MUA})]$, the positions of precipitation points for different values of α_{sol} are related by $\chi^P_\alpha = \chi^P_0 \cdot \eta^{MUA}/(1 + \chi^P_0 \cdot \eta^{MUA} - \chi^P_0)$, where χ^P_0 is the precipitation point of AuNPs soaked in pure MUA ($\alpha_{sol} = 0$). Therefore, the ratio of the equilibrium constants K^{MUO} and K^{MUA} can be determined from the slope of the dependence of $1/\chi^P_\alpha$ on α_{sol}: $1/\chi^P_\alpha = 1/\chi^P_0 + (1/\chi^P_0 - 1)(K^{MUO}/K^{MUA})\alpha_{sol}$ (Fig. 13c). Knowing the relative adsorption equilibrium constants, one can then easily prepare NPs of desired charges—such particles then constitute building blocks of "nanoionic" materials to be discussed later in Section 4.3.

4.2.2 Oppositely and like charged non-spherical nanoparticles in solution. Unlike charged macromolecules, nanoparticles can have their shapes and sizes easily controlled. The interactions between charged non-spherical particles can be fundamentally different – and more versatile in terms of self-assembly strategies—than those between spherical NPs. Take, for instance the interactions between oppositely charged spherical NPs and metallic nanorods, NRs. The distinguishing feature of the NRs is that while being coated with charged organics, their metallic cores are polarizable, with highest polarizability along the rod's long axis. This means that in addition to considering charge-charge interactions, one must also take into account the attractive charge-induce dipole forces. These forces depend on the concentration of counterions and the screening length. Specifically, when the concentration of ions in the surrounding solution is high, the polarizing effect of the NP on the NR is effectively screened, the induced dipole is small, and the interaction is dominated by the charge-charge component, which always prefers an arrangement whereby the NP is attached half-way along the NR's side. In sharp contrast, when the screening length is large (low concentration of ions), the NP induces an appreciable dipole in the NR and this charge–dipole interaction causes the NP to attach at the "tip" of the NR. Overall, by controlling the screening length in the system, it is possible to non-invasively position the NP at either the end (Fig. 14a) or the side (Fig. 14b) of a nanorod. A similar strategy can be used to manipulate particles of other shapes, for instance rods and triangles shown in Fig. 14c, d.

An even more striking manifestation of the importance of the charge-induced dipole effects is illustrated in Fig. 14 e,f. Here, both the NPs and the NRs are like-charged. When the screening length is large, the charge induced dipole attraction actually

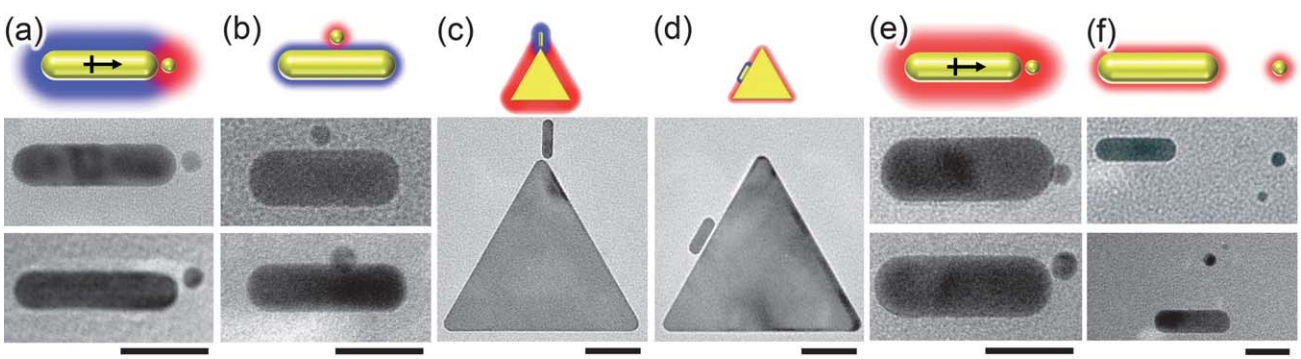

Fig. 14 Site-selective electrostatic self-assembly of oppositely- and like-charged particles. Schemes and representative TEM images of **(a, b)** Oppositely charged nanoparticle/nanorod (NP/NR) systems. The "tip" arrangements shown in (a) is observed for large-screening length where charge-induced dipole interactions are appreciable (here, for TMA NPs/MUA NRs pair with $\kappa^{-1} \approx 10$ nm). The "side" arrangement in (b) is observed for small screening lengths (TMA NPs/MUA NRs, $\kappa^{-1} \approx 0.6$ nm). **(c, d)** Similar trends hold for nanotriangle/nanorod (NT/NR) systems (here TMA NTs/MUA NRs) with both **(c)** large and **(d)** small screening lengths. **(e, f)** Like-charged NP/NR systems. **(e)** for large screening lengths (here, TMA NPs/TMA NRs, $c_S \approx 1$ mM, $\kappa^{-1} \approx 10$ nm) where charge-induced dipole attraction overcomes electrostatic repulsion, the particles aggregate in a "tip" arrangement; **(f)** when screening length is small (TMA NPs/TMA NRs, $c_S \approx 250$ mM, $\kappa^{-1} \approx 0.6$ nm) and induced dipoles are negligible, repulsive electrostatic interactions dominate and the particles repel one another. In the schemes, the screening length is proportional to the thickness of the halos around the particles; red and blue colors indicate, respectively, positive and negative particle polarity. Scale bars for NR/NP and NT/NR systems are 20 nm and 50 nm, respectively. Reprinted with permission from ref. 99. Copyright 2010 American Chemical Society.

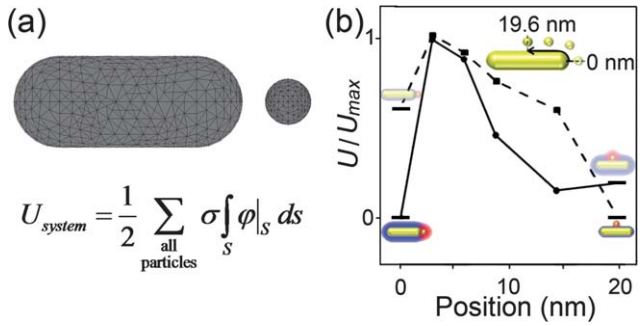

Fig. 15 **(a)** Finite Element Method (FEM) can be used to solve for the potential around more complex geometries by representing these objects as a 3-dimensional mesh. After solving the PB equation with the appropriate boundary conditions (see Section 2.3) the surface potential can be numerically integrated over the surface and the energy of the system/configuration can be found. **(b)** Energy diagrams can be obtained from FEM calculations for various particle orientations and experimental conditions. Here, we show the normalized energy as a NP moves along the contour of a NR at either large or small screening lengths. As observed in the corresponding experiments (see Fig. 14), the FEM method predicts that a 'tip' assembly is preferred when the electrostatic interactions are unscreened, but the 'side' assembly becomes most favorable when the screening lengths are short. Reprinted with permission from ref. 99. Copyright 2010 American Chemical Society.

overcomes the like-charge attraction and the particles aggregate in the "tip" configuration. When, however, the screening length is decreased (by the addition of salt), the charge-charge repulsion has the upper hand and the assembly falls apart.

A few comments are due regarding the theoretical treatment of electrostatics in systems of non-spherical particles. As might be expected, analytical solutions of the PB equation for such low-symmetry systems are difficult and in many cases prohibitive. Consequently, one can either resort to gross approximations—for instance, treat interacting particles as point charges and/or point dipoles (see ref. 99 for details)—or else use numerical packages such as COMSOL Multiphysics (previously known as FEM Lab) whereby the interacting objects are represented as a three-dimensional triangulated mesh (Fig. 15a) and the PB equation with appropriate boundary conditions is solved by the Finite Element Method.[205] FEM method is computationally intensive but can handle particles of any shape. It is important to remember, however, that while most software packages triangulate particle surfaces automatically, the quality of triangulation should be checked by the user to make sure that regions of higher curvature have finer mesh (this avoids the formation of sharp 'edges' in the mesh, which can prevent the convergence on a solution). When properly setup, FEM methods give solutions that have accuracy typically within a fraction of a per-cent from analytical ones (in problems where analytical solutions are available). An example of the results from such a calculation is shown in Fig. 15b, where an energy diagram is created for the NR/NP system discussed above. The energy of the system can be computed for the NP moving along the contour of the NR to show the configuration of lowest energy for each screening length.

4.2.3 Aggregates of charged nanoparticles—coda. The nature of electrostatic interactions between charged nano-objects is often counterintuitive, especially between non-spherical particles where charge-induced dipole interactions are important. In such cases, nanopositioning and like-charge attraction can be controlled by the ionic strength of the solution, which dictates the screening length.

4.3 Nanoscale self-assembly driven by electrostatic interactions

As we have seen in the previous Section, the nature (attractive/repulsive), the range and the directionality of electrostatic interactions at the nanoscale can be tailored by adjusting the shapes and sizes of the NPs as well as the characteristics of the surrounding medium. With such a flexible control, electrostatic forces are well suited to mediate assembly of nanostructured materials. In this section, we will review some recent examples of structures held by electrostatic forces, ranging from one dimensional chains to three-dimensional crystals and even crystals-within-crystals.

4.3.1 Self-assembly of 1D chains and 2D sheets. An interesting class of 1D and 2D nanostructures has been described by Kotov and co-workers. These authors have shown that ~2.5 nm CdTe quantum dots, when functionalized with negatively charged thioglycolic acid (TGA), spontaneously assemble into long "pearl-necklace" chains,[33,206] but when functionalized with positively charged 2-(dimethylamino)ethanethiol (DMAET), form large-area, free-floating sheets.[33,207] The origin of this dual-mode assembly was attributed to a delicate interplay of various types of interparticle interactions and to the unique shape of nanocrystals. Specifically, these crystals are tetrahedrons in which some of the high-free-energy apexes are truncated. Both experiments and semiempirical quantum mechanical calculations indicate that the presence of truncations can translate into the distribution of charged ligands over the particle's surface such

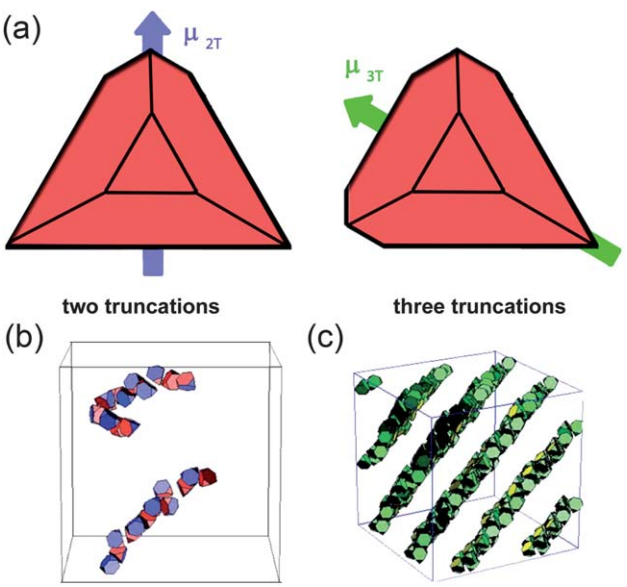

Fig. 16 **(a)** The direction of dipole moments in tetrahedral CdTe nanoparticles with two and three truncations. **(b, c)** Computer simulations of the assembly of CdTe nanoparticles into **(b)** chains and **(c)** sheets. From ref. 207. Reprinted with permission of AAAS.

that the particle has a net dipole moment (up to ~100 Debye) – the direction of the dipole depends on the number of truncations (Fig. 16a), and its magnitude scales with the degree of truncation.

The formation of "pearl-necklace" 1D assemblies illustrated in Fig. 16b depended crucially on the interplay between charge-charge repulsions and dipole–dipole attractions. In particular, these structures form only when some of the charged ligands are desorbed from CdTe surfaces such that the charge-charge repulsions are weakened. With careful control of this process, the dipole–dipole interactions remain significant and commensurate with charge-charge repulsions (both a few kT). The well-known preference of dipoles to align then leads to the formation of particle chains that can be up to 1μm long and exactly one nanoparticle wide.

The same CdTe nanoparticles but stabilized with positively charged DMAET rather than negatively charged TGA assemble into 2D sheets (Fig. 16c).[33] DMAET ligands have charges of magnitudes smaller than TGA and also bear methyl groups which contribute to attractive hydrophobic interactions between the NPs. The direction of the dipole, attractive hydrophobic interactions and repulsive electrostatic interactions between NPs then all contribute to the assembly of planar sheets. Calculations confirm that this type of assembly is the lowest-energy configuration characterized by antiparallel orientation of nearby dipoles, and is crucially dependent on the electrostatic effects. For instance, without electrostatic repulsions, the particles are predicted to form 3D aggregates with random arrangement of the CdTe components.

4.3.2 2D surface coatings made of oppositely charged nanoparticles. Nanoparticulate surface coatings are amongst the most important nanostructured materials. Depending on the nature of the constituent NPs, these coatings can exhibit a range of useful properties including electronic, optical,[38] mechanical[208] and biological.[209] Electrostatics based on charged NPs provides a facile route to the formation of coatings whose unique feature is that they form on a variety of materials including glasses, semiconductors, or polymers (including "inert" ones such as polypropylene[210]) without the need for chemical/covalent ligations. In one method, the coatings are deposited from solutions containing oppositely charged NPs (see Section 4.2) – while stable in dilute solution, these NPs adsorb onto any surface presenting residual charge developed *via* spontaneous oxidation in air or by plasma treatment. Interestingly, adsorption is cooperative[211] in the sense that it requires the presence of particles of opposite polarities (like-charged NPs adsorb only marginally due to interparticle repulsions). The NPs initially "seed" the surface slowly, but as the adsorption progresses, its rate accelerates before finally leveling off when the surface becomes crowded; overall, absorption kinetics is sigmoidal. Qualitatively, the cooperativity in this system is due to the fact that the ± NPs already present on the surface facilitate attachment of even more particles, much in the same way as a "seed" of an ionic crystal promotes further crystal growth. An interesting feature of the NP adsorption mechanism is that the process self-terminates after the deposition of exactly a monolayer of nanoparticles. This monolayer comprises equal numbers of positively and negatively charged NPs and thus presents no net charge that could facilitate attachment of more NPs. On the other hand, when the deposited monolayer is washed with base (to deprotonate some of the ligands on the NPs), it regains its net charge and ability to promote further NP adsorption—in this way, multilayered NP coatings can be deposited.

Referring a reader interested in mechanistic theoretical details to ref. 200, 211 we highlight some practical advantages of the method. First, since deposition leads to monolayers incorporating equal numbers of "+" and "−" NPs and is driven by the electrostatics alone (and not by the nature of the NPs' cores), it is possible to prepare the coatings made of different combinations of materials. For example, a solution of 25% of AuTMA NPs, 25% of AgTMA NPs and 50% of PdMUA NPs (TMA = SH-$(CH_2)_{11}$-$N(CH_3)_3^+$; MUA = SH-$(CH_2)_{11}$-COO^-) deposits a coating whose elemental composition is 1 : 1 : 2 (see Fig. 17a for this and other examples). Second, because deposition is solution based, it can give uniform coatings over curved surfaces, including inner surfaces of vials and tubing. Fig. 17b shows examples of AgNP(+)/AgNP(−) coatings formed inside of Tygon tubing used in medical applications—owing to the bacteriostatic nature of silver nanoparticles, the tubing remains sterile in the presence of both Gram positive *S. Aureus* and Gram negative *E. Coli* bacteria.[210] Finally, the ordering of the coatings can be improved by performing the deposition in the presence of AC fields that "jiggle" the charged particles and drive their close packing (Fig. 17c). The electrohydrodynamic phenomena accompanying AC forcing are described in detail in ref. 212.

4.3.3 Binary nanoparticle superlattices. Historically, ordered nanoparticle lattices have often been prepared by solvent evaporation leading to entropically-driven NP packing.[169] Shevchenko *et al.* demonstrated that an unprecedented variety of binary nanoparticle superlattices (BNSL) comprising magnetic, metallic, and semiconductor nanoparticles[32] can be obtained by combining van der Waals, steric, dipolar and entropic forces with electrostatic interactions. Remarkably, many of these lattices were non-closed-packed and could not be obtained without electrostatic forces.

In their experiments, Shevchenko *et al.* used different combinations of metallic and semiconductor NPs (PbSe, PbS, Au, Ag, Pd, Fe2O3, CoPt3, and Bi) stabilized by the addition of different amounts of surfactants like oleic acid (OA) and tri-n-octylphosphine oxide (TOPO) that can modify the NPs surface charge. Electrophoretic mobility (μ_e) measurements without excess of any capping ligands demonstrated that these NPs have few fundamental charges each. The mobility distribution curve showed several distinct peaks corresponding to particle populations with −1, 0, 1 and 2 fundamental charges. However, by introducing an excess of TOPO and/or OA it was possible to prepare samples with NPs of precisely defined charge. While the mechanism behind this charge adjustment is not fully understood, it is an interesting illustration of controlling charges by means other than the ubiquitous self-assembled monolayers.

A case in point are PbSe NPs coated with oleate ligands, $C_{17}H_{33}COO^-$, attaching to the Pb atoms on the particle's surface. When oleic acid is added to the solution in excess, some oleate species on the NP surface can be protonated and desorbed, leaving behind positively charged surface sites. The excess OA can also protonate the negatively charged oxidized Se sites (forming upon exposure to atmospheric oxygen), again

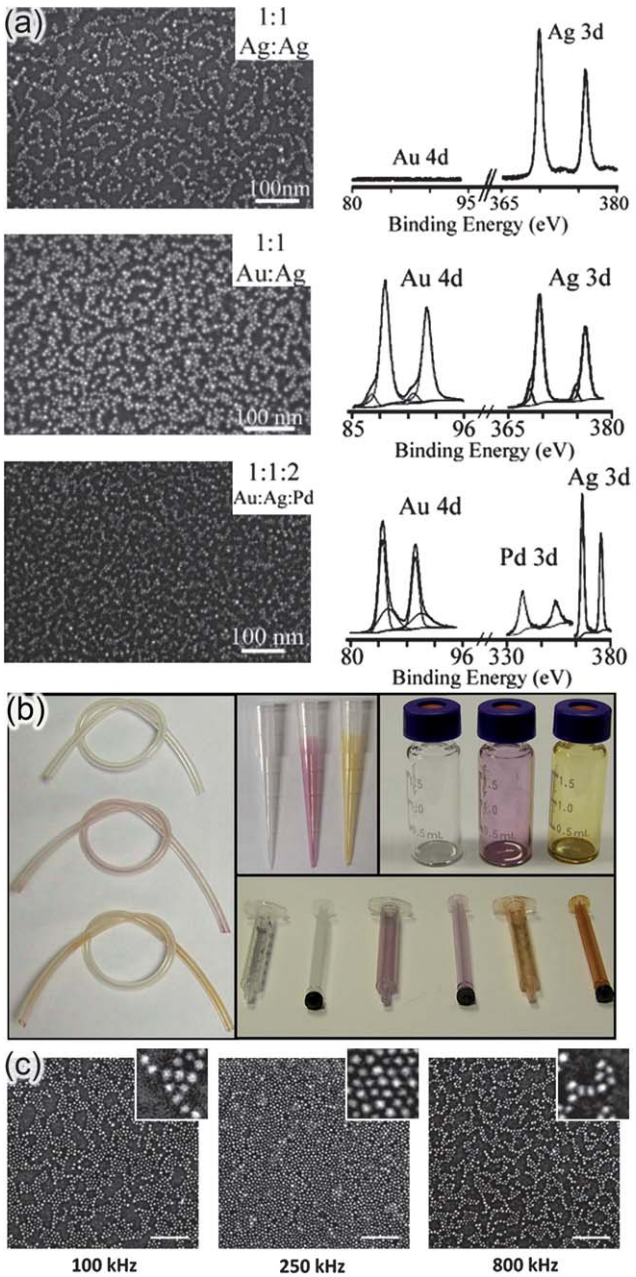

Fig. 17 **(a)** SEM images (left panel) and XPS spectra showing structure and metal composition (right panel) of coatings composed of oppositely charged NPs having same or different metal cores: AgMUA/AgTMA (top), AuMUA/AgTMA (middle) and AuTMA/AgTMA/PdMUA (bottom). TMA = SH-$(CH_2)_{11}$-$N(CH_3)_3^+$; MUA = SH-$(CH_2)_{11}$-COO^-. **(b)** Examples of medically relevant components coated with bacteriostatic NP monolayers of oppositely charged nanoparticles: Tygon-R tubing, polypropylene micropipette tips, glass vials, and polypropylene syringes. Yellow-orange coatings are made of AgMUA/AgTMA; pink coatings, from AuMUA/AgTMA. Uncolored pieces are shown for reference. **(c)** SEM images of typical binary AuMUA/AgTMA NPs coatings deposited with different AC frequencies ranging from 100 to 800 kHz. All samples were prepared at the same electric field strength of 150 V cm^{-1} (*i.e.*, 5 V across 340 μm) and 15 min of field application. Scale bars are 100 nm; the insets are 50 nm × 50 nm. Reprinted with permission from ref. 210. Copyright 2010 American Chemical Society.

increasing particle's net positive charge. In contrast, TOPO charges the NPs negatively, likely because of its ability to complex (positively charged) lead ions and abstract them from the NP surface, leaving behind an excess of negatively charged Se sites.

With charge magnitudes controlled to within one fundamental charge per nanoparticle, Shevchenko *et al.* were able to crystallize various BNSLs. For example (Fig. 18), 6.2 nm PbSe and 3.0 nm Pd nanoparticles formed orthorhombic AB- and AlB_2-type lattices in the presence of oleic acid (under these conditions, metallic and semiconductor NPs were oppositely charged), while addition of TOPO caused the change of the BNSL structure to $NaZn_{13}$-type (negative charge on metallic nanoparticles was neutralized by TOPO, and positively charged semiconductor nanoparticles became negatively charged).

It is worth mentioning that electrostatic interactions not only stabilize the superlattices, but also determine their stoichiometry. For the growth of large, ordered areas, the electroneutrality condition has to be fulfilled – that is, the positive charges should compensate the negative ones or else the local electrostatic energy of the lattice becomes unfavorable and further growth self-terminates. This was indeed seen in experiments showing relatively small regions of different types of BNSLs nucleating on the same substrate, but not exceeding 100 NPs, while stable structures with compensated charges comprised up to tens of millions of NPs.

4.3.4 Superlattices of nanoplates. In contrast to the crystallization of small, spherical NPs,[213,214] self-assembly of components of lower symmetries (rods,[215–217] plates,[216] *etc.*[218]) remains an experimental challenge. For such particles, crystallization is often hindered by strong van der Waals (vdW) attractions[169] that lead to indiscriminate aggregation/flocculation of the particles rather than to orientation-specific self-assembly. This is especially true in the case of high-aspect ratio (width:thickness) polygonal nanocrystals that tend to "stick" along their flat faces with no long-range order. We have recently shown that for such systems electrostatics can facilitate particle ordering into either 2D lattices or 3D crystals – paradoxically, however, self-assembly is then facilitated by *repulsive* interparticle interactions that weaken van der Waals attractions and effectively serve as a "molecular lubricant" that allows the particles to fine-tune their mutual orientations.

Our work[105] focused on the assembly of metallic nanotriangles, NTs, that are of particular interest due to the presence of sharp edges where electro-magnetic fields are concentrated into "hot-spots" which enhance SERS (Surface Enhanced Raman Spectroscopy) sensing abilities.[219–223] In our experiments, the as-prepared NTs were stabilized by hexadecyltrimethylammonium bromide (CTAB). For these particles, crystallization protocol based on solvent evaporation led to disordered aggregates as illustrated in Fig. 19a. When, however, the NTs were functionalized with charged ligands such as N,N,N-trimethyl(11-mercaptoundecyl) ammonium chloride, TMA, they crystallized into large arrays several layers thick (Fig. 19b). Furthermore, when the charge on the NTs was further increased by intercalation of charged surfactants into charged SAMs, the triangles formed large-area monolayers (Fig. 19c).

While exact calculations of free energies (*i.e.*, including entropic effects) for this system are prohibitively complicated,

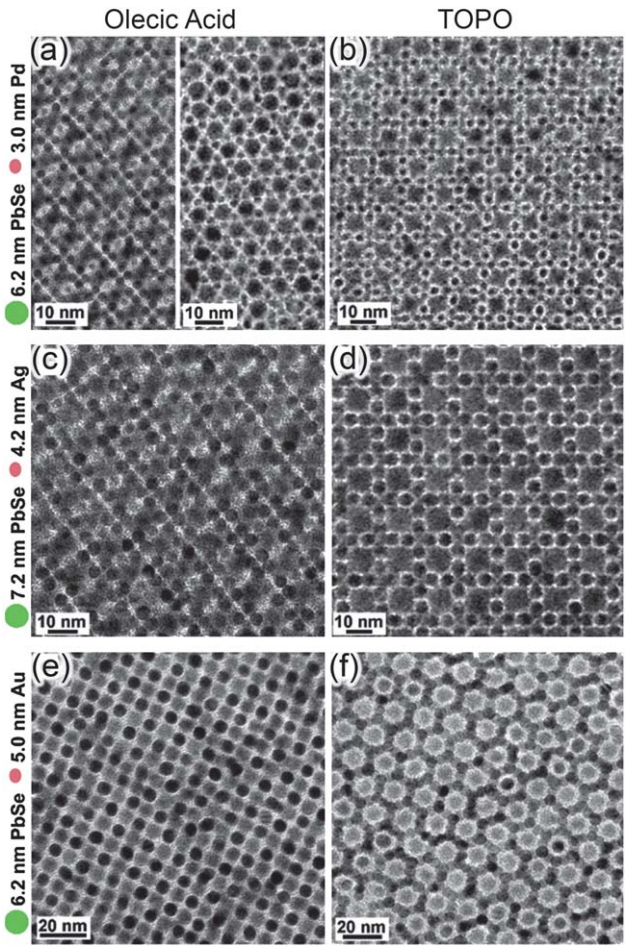

Fig. 18 TEM images of BNSLs assembled in the presence of OA (left column) and TOPO (right column). **(a)** 6.2 nm PbSe and 3.0 nm Pd nanoparticles self-assembled into orthorhombic AB- and AlB_2-type BNSLs in the presence of OA. **(b)** Same nanoparticles form $NaZn_{13}$-type BNSL in the presence of TOPO **(c, d)** 7.2 nm PbSe and 4.2 nm Ag nanoparticles self-assembled into orthorhombic AB and cuboctahedral AB_{13} BNSLs, respectively. **(e, f)** 6.2 nm PbSe and 5.0 nm Au nanoparticles self-assembled into CuAu-type and $CaCu_5$-type BNSLs, respectively. Reprinted by permission from Macmillian Publishers Ltd: Nature, 2006.[32]

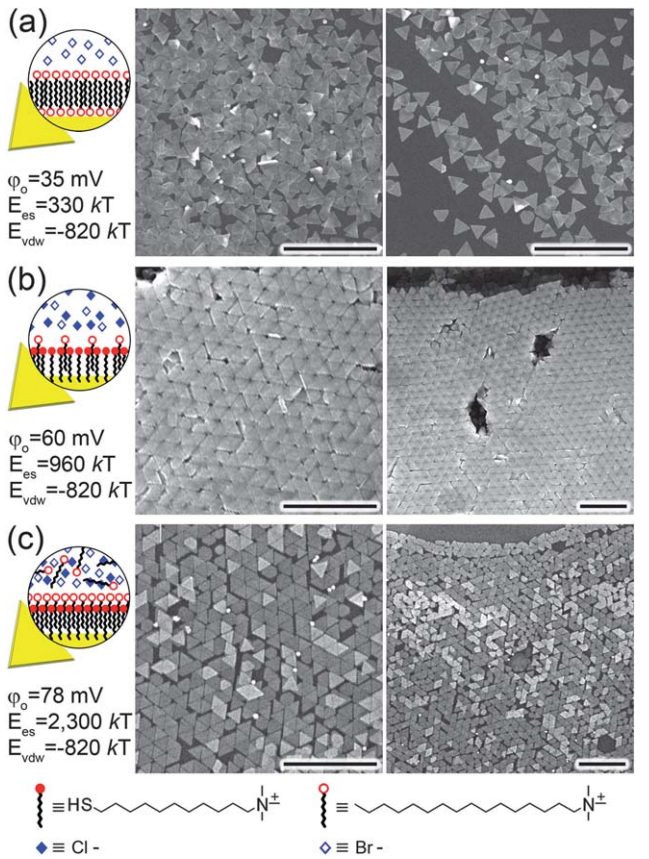

Fig. 19 **(a)** Gold nanotriangles, AuNTs, stabilized only by excess cetyltrimethylammonium bromide (CTAB) surfactant (20 mM CTAB, surface potential $\varphi_o = 35$ mV, $E_{el} \sim 330\ kT$) form disordered aggregates. **(b)** Triangles functionalized with positively charged SAMs (here, of TMA thiols) and with only small quantities of CTAB surfactant present (<1 mM CTAB, $\varphi_o = 60$ mV, $E_{el} \sim 960\ kT$) organize into large, ordered multilayers. **(c)** AuNTs stabilized with TMA SAMs and in the presence of excess CTAB (20mM CTAB, $\varphi_o = 79$ mV, $E_{el} \sim 2{,}300\ kT$) give large monolayer arrays. All scale bars = 1 μm. Reprinted with permission from ref. 105. Copyright Wiley-VCH Verlag GmbH & Co. KGaA, 2010.

the experimental trends can be rationalized based on the interplay between van der Waals (vdW) attractions and electrostatic repulsions. The vdW forces increase with the area of contact and are the strongest when the NTs are stacked "on top" of one another. Approximating the triangles as semi-infinite plates of finite thickness, the energy of these interactions is $E_{vdW} = -A[1/d^2 - 2/(d+h)^2 + 1/(d+2h)^2]/12\pi$,[178] where $A \sim 10^{-19}$ J[224] is the Hamaker constant for gold across water, d is the distance between the two plates (here, about two times SAM thickness, ~2.8 nm[28]), and $h \sim 8.7$ nm is the thickness of the plates (see Table 2). For the NTs we used, the maximal surface area of contact (when two triangles are stacked perfectly) is ~11,000 nm^2, and the corresponding $E_{vdw} \sim -820\ kT$.

The vdW energies are partly offset by electrostatic repulsions. The electrostatic energy, per unit area, between two semi-infinite plates with equivalent potentials is[225] $E_{el} = \varepsilon\varepsilon_o k\varphi_o^2(1 - \tanh(kd/2))$, where $\varphi_o$is the constant potential at the plate's surface[226] (see also Table 1). To determine φ_o, the by-now familiar linearized Poisson-Boltzman (PB) equation, $\nabla^2\varphi = \kappa^2\varphi$, is solved with the relation between charge density and potential, $\sigma = d\varphi_o/dx$, applied at the boundaries $x = 0$ and $x = d$ (coordinate x is perpendicular to the plates' surfaces). Solving yields $\sigma = \varepsilon\kappa\varphi_o(\coth(\kappa d) - \operatorname{csch}(\kappa d))$ which relates the surface potential to the charge density (determined from electrophoretic mobility experiments;[227] $\sigma = \mu\nu\kappa$,[225] where μ is the mobility, ν is the viscosity of the medium, and κ^{-1} is the electrostatic screening length of a given solution). Once the surface potential of the particles is known, the electrostatic energy of the assembly can be calculated. For NTs stabilized by CTAB alone, the surface potential was measured at $\varphi_o = 35$ mV, and the calculated energy of electrostatic repulsion is $E_{el} \sim 330\ kT$. Since this energy is significantly smaller than E_{vdw}, the process of assembly is dominated by vdW forces leading to rapid and indiscriminate aggregation. This situation changes for TMA-functionalized NTs for which $\varphi_o = 60$ mV and $E_{el} \sim 960\ kT$ is commensurate with E_{vdw}. In this case, the "balance" between

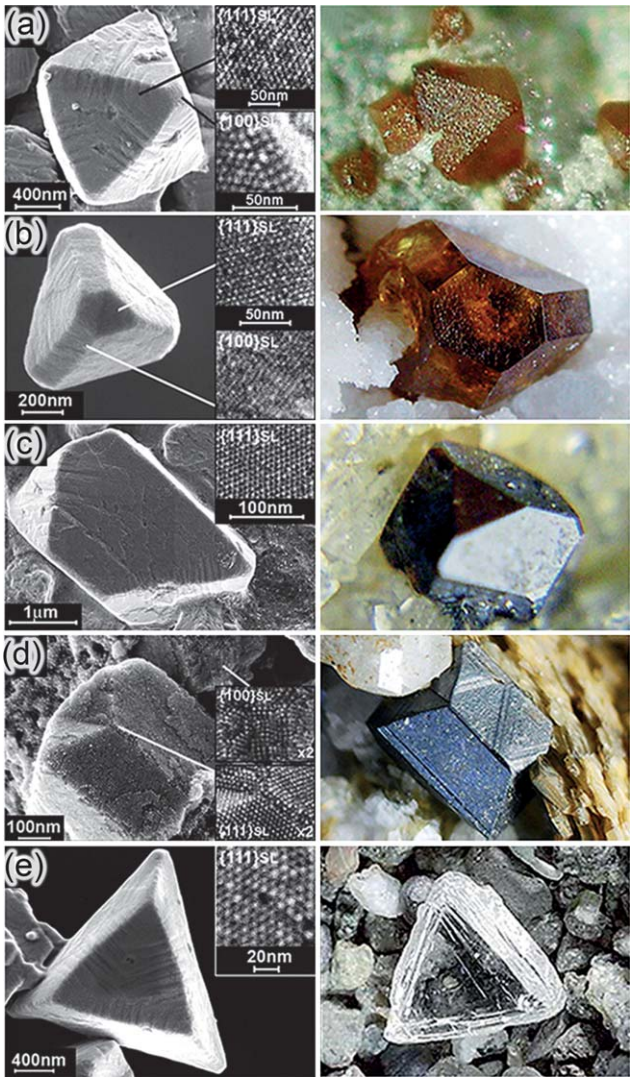

Fig. 20 The left column has the SEM images of diamond-like crystals formed from oppositely charged, 5 nm Au and AgNPs. Insets zoom on the particles on the crystals' faces. The right column has the zinc-blend crystals (lattice isostructural with diamond) with similar morphologies. From ref. 28. Reprinted with permission of AAAS.

electrostatic repulsions and the vdW attractions allows the NTs to adjust their mutual orientations during assembly leading to well-ordered, multilayer structures. Finally, when TMA SAM has extra charged surfactant intercalated, $\varphi_o = 79$ mV, and $E_{el} \sim 2{,}300\ kT$ —then, the net interaction between the NTs is repulsive and the stacking of the NTs into multilayers is energetically unfavorable. At the same time, the triangles are large and massive enough that they sediment from solution onto the deposition substrate where they form monolayers.

The main and probably counterintuitive insight from these studies is that electrostatic repulsions can actually facilitate nanoscale self-assembly by softening strongly attractive interparticle potentials. It is a useful trick to remember!

4.3.5 3D nanoparticle crystals. So far, we have described electrostatic assembly schemes that require the presence of a deposition substrate. Naturally, it would be desirable to extend

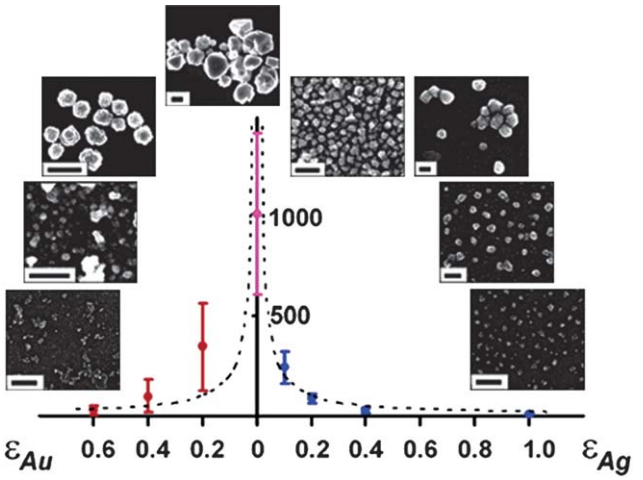

Fig. 21 Size control during crystallization of equally sized, ~5 nm AuMUA and AgTMA nanoparticles at pH 10. The graph plots average sizes (in nm) of crystals grown with different amounts of excess gold or silver NPs ($\varepsilon_{Au}/\varepsilon_{Ag}$, respectively). Vertical bars denote the ranges of the crystals sizes observed; insets have the SEM images of typical crystals (scale bars are 100 nm for $\varepsilon_{Au} = 0.6$ and $\varepsilon_{Ag} = 0.2$, 0.4, 1.0, and 1 μm for all other experiments). Dashed line is a theoretical fit to the expected $d \propto 1/\varepsilon_{Ag}$ dependence. Reprinted with permission from ref. 249. Copyright 2007 American Chemical Society.

these schemes to three-dimensional nanomaterials. However, the task of organizing charged NPs into 3D supracrystals is not a trivial one, since the relatively strong electrostatic forces often lead to flocculation and rapid precipitation rather than crystallization (for discussion of pertinent chemical potentials of various aggregated phases, see ref. 28). The key to successful crystallization is, as with molecular ions, to make the process very slow. In a class of systems Kalsin *et al.* developed, oppositely charged ~5 nm NPs are crystallized from a mixture of water and DMSO. When the "good" solvent (water) is slowly being evaporated at 65 °C, the NPs become less readily soluble and crystallize into sharply-faceted crystals, each comprising several millions of nanoparticles (Fig. 20).

While for equally sized and oppositely charged NPs one might expect – by analogy to inorganic ions – the crystal structure to be either NaCl or CsCl, nanoscale electrostatics again defies the intuitive. Surprisingly, the NPs crystallize into diamond-like structure, in which each NP is surrounded by four tetrahedrally arranged neighbors. Although in the diamond lattice each NP forms only $n = 4$ favorable "±" contacts (*versus* $n = 6$ in NaCl and $n = 8$ in CsCl), the like-charged particles in this open-lattice structure are farther apart than in the closed-packed NaCl or CsCl. Then, because the screening length around the NPs is commensurate with the particle diameters, the repulsions between like-charged next-nearest-neighbors in the diamond lattice are screened and effectively do not contribute to the unfavorable electrostatic energy of the crystal. Colloquially put, by "opening up" the structure one looses the favorable "±" energy, but saves on the "+/+" and "−/−" unfavorable contributions.

The sizes of the crystals can be controlled from several tens of nanometres up to several microns (see Fig. 21) by the addition of excess NPs of either polarity. The measurements of the

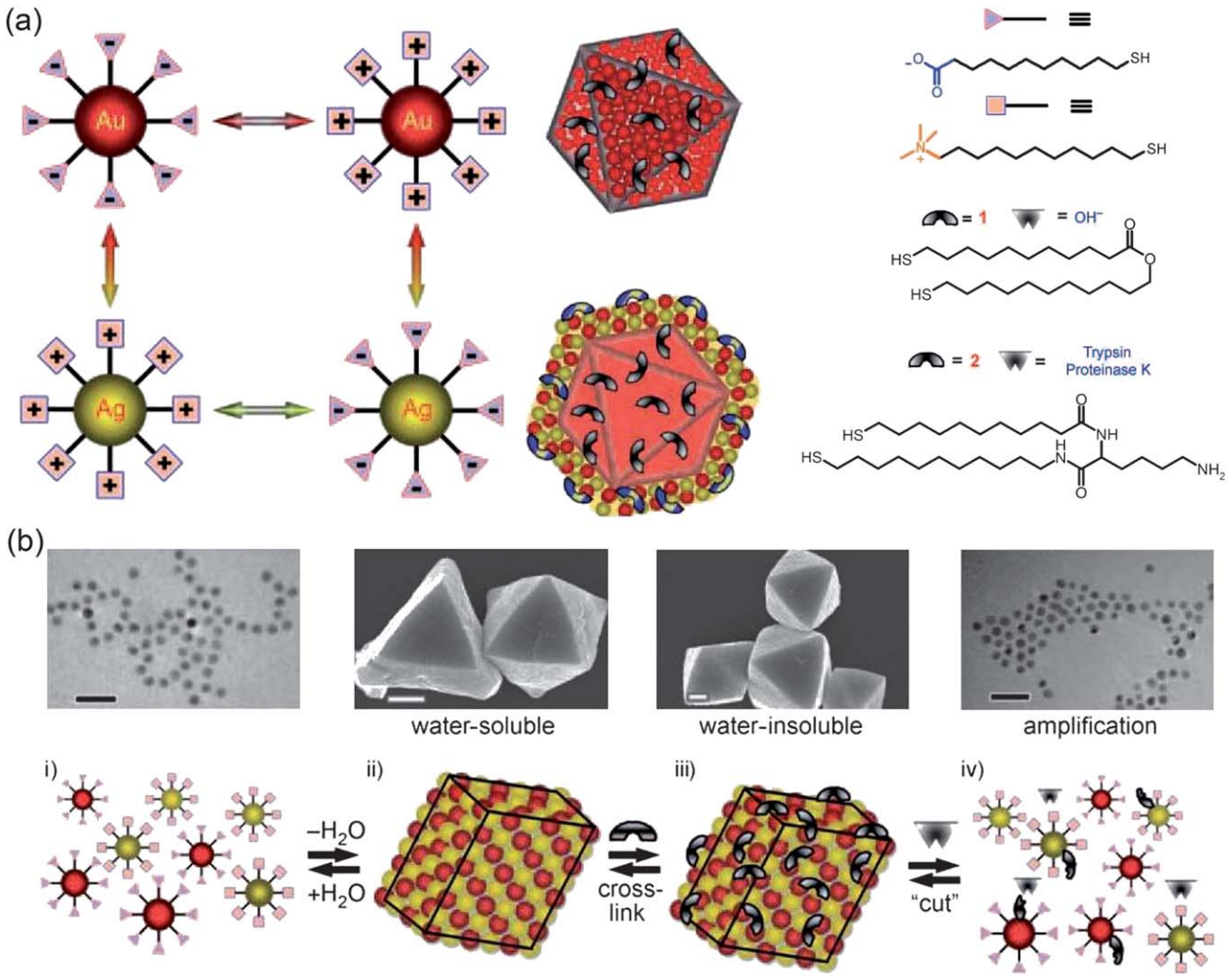

Fig. 22 **(a)** Schematic representation of nanoparticles, crystals, and core-shell ("Russian Doll") crystals used for amplified sensing. The fornulas on the right give the structures of the thiols coating the NPs, and also of two dithiols used to crosslink the crystals. One of the dithiols shown can be "cut" by hydroxyl ions; the other is cut by enzymes such as Trypsin or Proteinase K. **(b)** Procedure of amplified chemical sensing using nanoparticle supracrystals. Crystals self-assemble from oppositely charged NPs (*i*) and are soluble in water (*ii*). These crystals gain permanence and become water-insoluble when they are cross-linked with dithiols containing cleavable groups (see examples in a) (*iii*). When a specific analyte is added, the cross-links are chemically cut, and the crystals disintegrate into individual nanoparticles (*iv*). Reprinted with permission from ref. 228. Copyright Wiley-VCH Verlag GmbH & Co. KGaA, 2010.

ζ- potential indicate that the excess NPs "terminate" crystal growth by forming protective shells around the growing aggregates (see Section 4.2.1) – although the particles in these shells are all like-charged, the interactions between them are effectively screened, and the shells are stable.

It should be noted that crystallization of particles having different sizes and or charges remains problematic. In the former case, the NPs prefer to phase separate rather than co-crystallize. In the latter, the NPs often precipitate even if the charge ratios are small rational numbers – the reasons for this behavior are still not fully understood.

4.3.6 Chemical amplifiers and "Russian Doll" nanoparticle crystals. Three-dimensional crystals made of charged nanoparticles we have seen in the previous Section are soluble in water. When, however, these crystals are placed in a solution of dithiol molecules, HS-$(CH_2)_n$-SH, the thiol groups covalently crosslink the nearby particles on the crystal's surface and thus make these crystals stable in aqueous media.[228] The crystals reinforced in this way offer some unique opportunities for engineering nanostructured materials. When stabilized by analyte-specific cross-linkers (dithiols with groups prone to cleavage upon reaction with analyte molecules) such crystals are still stable in pure water, but rapidly dissolve when specific molecules are present in solution (see ref. 228 and Fig. 22). Each of such crystals can be depicted as a "balloon" with a thin protecting skin (composed of few layers of NPs cross-linked on the crystal's surface), while the vast majority of NPs inside it remain uncrosslinked and thus water soluble. Upon addition of specific analyte which "cuts" the cross-linkers, millions of individual NPs from inside of the crystal are liberated. These NPs adsorbing strongly in the visible regime give rise to pronounced color

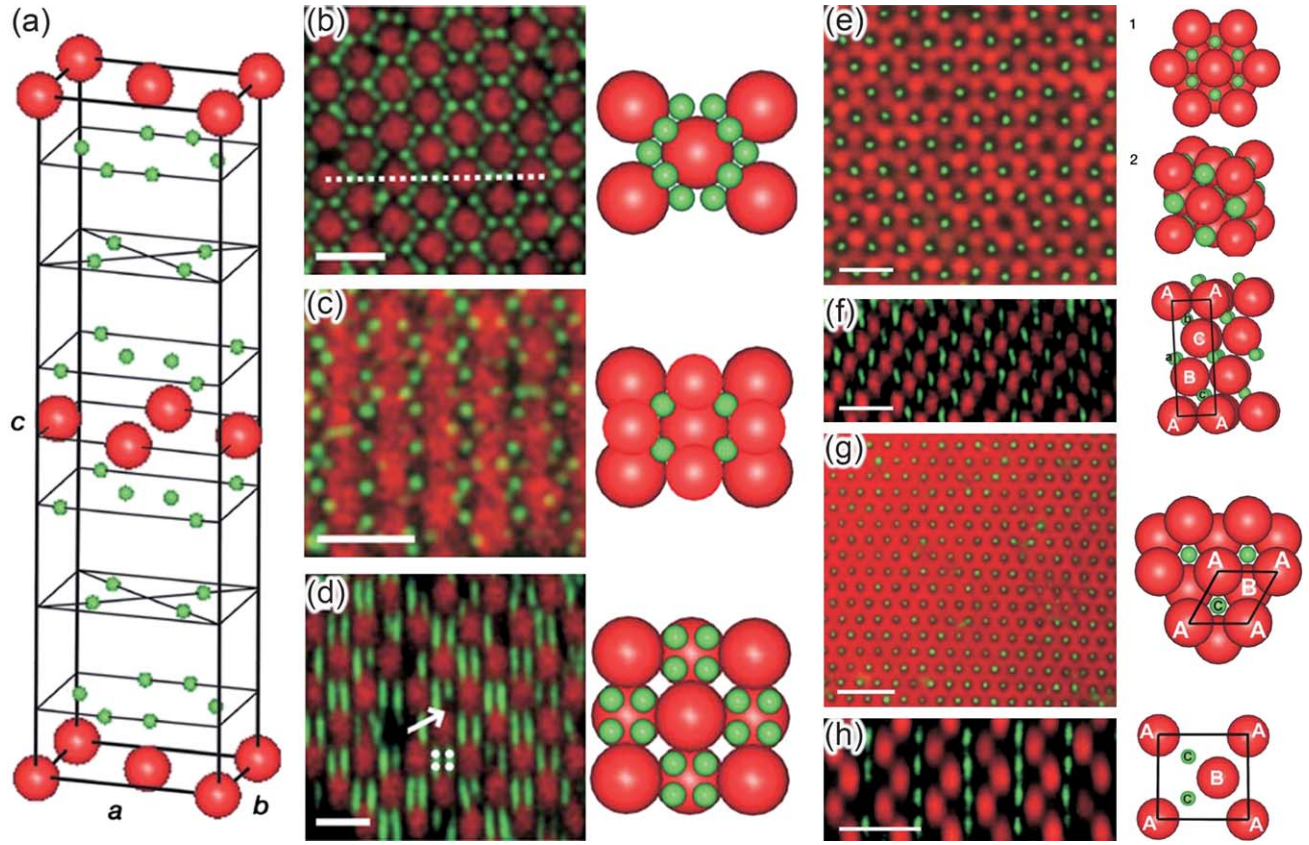

Fig. 23 **(a–d)** AB_6-type binary crystals. Positive (green, radius 0.36 μm) and negative (red, 1.16 μm) PMMA-particles in TBAB-containing CHB-decalin, forming a structure with AB_6 stoichiometry. **(a)** Unit cell and **(b–d)** confocal images and models of different *ab*-projections. The arrow indicates a "missing" particle. All scale bars are 4 μm. **(e–h)** AB-type binary crystals. Charged (red, radius 1.16 μm) and uncharged (green, 0.36 μm) PMMA-particles in CHB-decalin. Confocal images of **(e, f)** NaCl-type- and **(g, h)** NiAs-type crystal. Reprinted by permission from Macmillian Publishers Ltd: Nature, 2003.[30]

change, easily observed with a naked eye. The most important feature of this system is the amplification of the disassembly process – only few molecules of analyte are needed to "cut" several "holes" in the crystal's "skin" in order to liberate several millions of nanoparticles.

The same concept can be extended to "nanoionic" core-shell crystals. In this case, NP crystals stabilized with cross-linker "A" can be used as seeds for "epitaxial" growth of an additional crystalline layer (see Fig. 22a). Such crystals can then be again stabilized with dithiol crosslinkers, "B". As formed "Russian doll" NP crystals with the core and the shell stabilized with different types of dithiols allow for stepwise release of the outer and the inner NPs (upon exposure to analytes cutting, respectively, dithiols B and A). One practical application of these nanostructures could be in targeted drug delivery whereby the crystals release parts of their NP cargo only if they travel through specific concentration "landscapes" of the analytes (see ref. 228 for details).

4.3.7 Ionic colloidal crystals. Our discussion would be incomplete without highlighting the recent and exciting developments in the assembly of charged colloids. While, technically speaking, these particles do not qualify as nanoparticles (by NSF definition, "nano" pertains to objects smaller than 100 nm[229]), these submicrometer particles allow for precise tailoring the balance between electrostatic and vdW forces as well as for direct visualization of the assembled structures (*e.g.*, by confocal microscopy[230]).

Many of these systems were developed by the van Blaaderen group and comprised polymethylmethacrylate (PMMA)[231] and/or silica[30] particles in a mixture of bromocyclohexane and *cis*-decaline that matches the refractive index of the particles and eliminated van der Waals forces.[231] The magnitudes and the range of electrostatic interactions were controlled by the addition of a salt like tetrabuthylammonium bromide (TBAB). In apolar solvents, TBAB could not only regulate the screening length, but also reverse the polarity of PMMA particles from positive to negative at moderate salt concentrations (see ref. 232, 233 for details); silica particles were always negatively charged. Electrophoretic mobility experiments allowed estimating surface charge densities on the particles (*e.g.*, $Z = +110$ for 1.08 μm PMMA spheres in the presence of 60 μM TBAB) that were small enough to prevent irreversible particle aggregation.

Similarly-sized particles (~1 μm) crystallized into a CsCl type structure. Particles having considerably different sizes (L- large, S- small) could crystallize into several lattices depending on the experimental conditions. For example, at 120 μM concentration of TBAB, positive and negative PMMA particles ($d_+ = 0.36$ μm and $d_- = 1.16$ μm) formed a LS_6 lattice (see Fig. 23a–d) with large spheres arranged on a face-centered orthorhombic lattice, one

small sphere occupying each of the tetrahedral holes, and four small spheres located in each of the octahedral holes. Interestingly, the same system only in the slightly lower ionic strength crystallized into a LS_8 lattice. However, when no salt was added and small particles had no surface charge while large particles retained a small charge, the same system was found to crystallize into a LS structure of NaCl or NiAs type (see Fig. 23e–g).

We note that charged colloids offer some practical advantages over small, charged nanoparticles. For one, these particles can be made very monodisperse facilitating crystallization. They can be manipulated with optical tweezers[234] and can be arranged in desired patterns or structures with which to study epitaxial growth of colloidal crystals.[235,236] Also, they can be imaged by various microscopic modalities including confocal microscopy allowing for the direct reconstruction of the crystal's internal structure.

4.3.8 Nanoscale self-assembly driven by electrostatic interactions—coda. Electrostatic self-assembly at the nanoscale is far from trivial: Solvent, temperature, screening length, surface adsorption/intercalation of surfactants, counter/coion sizes and many other factors all contribute to the final outcome, which in some cases can be quite counterintuitive.

5. Conclusions and outlook

In summary, it is our hope that the examples presented in this Review, both theoretical and experimental, illustrate the versatility of electrostatic forces in controlling aggregation and self-assembly of nanoscale structures. While a significant amount of fundamental work has been done to quantify electrostatic interactions, the nanoscale still remains a relatively unexplored region where discoveries await. The role of nanoscience is to apply known forces in the design of new nanomaterials, but unfortunately, because of the complexities unique to this size regime, most theoretical justifications come *a posteriori*. This does not necessarily arise due to the inaccuracy or computational limitations of nano-electrostatic models (although this field continues to develop and improve), but rather to the large disconnect which often exists between those who develop the theory and those who perform the experiments. We hope that, at least in part, this Review will serve as a primer for experimentalists curious about the fundamentals of nanoscale electrostatics and for theorists curious about experimental practice. The rational engineering of nanoscale assemblies *via* electrostatic interactions is only possible when these two perspectives work closely together and support one another.

Acknowledgements

We acknowledge the assistance of Paul J. Wesson for his contributions to the discussion of continuum models, boundary conditions, and energies of interactions. This work was in part supported by the Materials Research Science and Engineering Center (MRSEC) funded by the National Science Foundation under NSF Award Number DMR-0520513 (D.A.W., and M.O.C). The work was also supported by the Non-equilibrium Energy Research Center (NERC) which is an Energy Frontier Research Center funded by the U.S. Department of Energy, Office of Science, Office of Basic Energy Sciences under Award Number DE-SC0000989 (B.K., and B.A.G.).

References

1 M. C. Daniel and D. Astruc, *Chem. Rev.*, 2004, **104**, 293–346.
2 T. S. Ahmadi, Z. L. Wang, T. C. Green, A. Henglein and M. A. El-Sayed, *Science*, 1996, **272**, 1924–1926.
3 S. H. Sun, C. B. Murray, D. Weller, L. Folks and A. Moser, *Science*, 2000, **287**, 1989–1992.
4 Y. G. Sun and Y. N. Xia, *Science*, 2002, **298**, 2176–2179.
5 R. Gref, Y. Minamitake, M. T. Peracchia, V. Trubetskoy, V. Torchilin and R. Langer, *Science*, 1994, **263**, 1600–1603.
6 C. R. Martin, *Science*, 1994, **266**, 1961–1966.
7 M. Bruchez, M. Moronne, P. Gin, S. Weiss and A. P. Alivisatos, *Science*, 1998, **281**, 2013–2016.
8 T. Trindade, P. O'Brien and N. L. Pickett, *Chem. Mater.*, 2001, **13**, 3843–3858.
9 E. A. Meulenkamp, *J. Phys. Chem. B*, 1998, **102**, 5566–5572.
10 S. H. Sun and H. Zeng, *J. Am. Chem. Soc.*, 2002, **124**, 8204–8205.
11 C. B. Murray, C. R. Kagan and M. G. Bawendi, *Annu. Rev. Mater. Sci.*, 2000, **30**, 545–610.
12 S. Vaucher, M. Li and S. Mann, *Angew. Chem., Int. Ed.*, 2000, **39**, 1793.
13 C. Burda, X. B. Chen, R. Narayanan and M. A. El-Sayed, *Chem. Rev.*, 2005, **105**, 1025–1102.
14 A. N. Shipway, E. Katz and I. Willner, *ChemPhysChem*, 2000, **1**, 18–52.
15 A. C. Templeton, M. P. Wuelfing and R. W. Murray, *Acc. Chem. Res.*, 2000, **33**, 27–36.
16 R. Elghanian, J. J. Storhoff, R. C. Mucic, R. L. Letsinger and C. A. Mirkin, *Science*, 1997, **277**, 1078–1081.
17 K. L. Kelly, E. Coronado, L. L. Zhao and G. C. Schatz, *J. Phys. Chem. B*, 2003, **107**, 668–677.
18 K. S. Lee and M. A. El-Sayed, *J. Phys. Chem. B*, 2006, **110**, 19220–19225.
19 W. P. McConnell, J. P. Novak, L. C. Brousseau, R. R. Fuierer, R. C. Tenent and D. L. Feldheim, *J. Phys. Chem. B*, 2000, **104**, 8925–8930.
20 L. J. Sherry, R. C. Jin, C. A. Mirkin, G. C. Schatz and R. P. Van Duyne, *Nano Lett.*, 2006, **6**, 2060–2065.
21 J. J. Storhoff, A. A. Lazarides, R. C. Mucic, C. A. Mirkin, R. L. Letsinger and G. C. Schatz, *J. Am. Chem. Soc.*, 2000, **122**, 4640–4650.
22 A. Nitzan and M. A. Ratner, *Science*, 2003, **300**, 1384–1389.
23 A. T. Bell, *Science*, 2003, **299**, 1688–1691.
24 M. Haruta, *Gold Bulletin*, 2004, **37**, 27–36.
25 R. Narayanan and M. A. El-Sayed, *J. Phys. Chem. B*, 2005, **109**, 12663–12676.
26 J. Y. Park, Y. Zhang, M. Grass, T. Zhang and G. A. Somorjai, *Nano Lett.*, 2008, **8**, 673–677.
27 N. Tian, Z. Y. Zhou, S. G. Sun, Y. Ding and Z. L. Wang, *Science*, 2007, **316**, 732–735.
28 A. M. Kalsin, M. Fialkowski, M. Paszewski, S. K. Smoukov, K. J. M. Bishop and B. A. Grzybowski, *Science*, 2006, **312**, 420–424.
29 W. Kung, P. Gonzalez-Mozuelos and M. O. de la Cruz, *Soft Matter*, 2010, **6**, 331–341.
30 M. E. Leunissen, C. G. Christova, A. P. Hynninen, C. P. Royall, A. I. Campbell, A. Imhof, M. Dijkstra, R. van Roij and A. van Blaaderen, *Nature*, 2005, **437**, 235–240.
31 S. Y. Park, A. K. R. Lytton-Jean, B. Lee, S. Weigand, G. C. Schatz and C. A. Mirkin, *Nature*, 2008, **451**, 553–556.
32 E. V. Shevchenko, D. V. Talapin, N. A. Kotov, S. O'Brien and C. B. Murray, *Nature*, 2006, **439**, 55–59.
33 Z. Y. Tang, Z. L. Zhang, Y. Wang, S. C. Glotzer and N. A. Kotov, *Science*, 2006, **314**, 274–278.
34 I. Hussain, Z. X. Wang, A. I. Cooper and M. Brust, *Langmuir*, 2006, **22**, 2938–2941.
35 R. Klajn, K. J. M. Bishop, M. Fialkowski, M. Paszewski, C. J. Campbell, T. P. Gray and B. A. Grzybowski, *Science*, 2007, **316**, 261–264.
36 M. M. Maye, J. Luo, I. I. S. Lim, L. Han, N. N. Kariuki, D. Rabinovich, T. B. Liu and C. J. Zhong, *J. Am. Chem. Soc.*, 2003, **125**, 9906–9907.

37 T. K. Sau and C. J. Murphy, *Langmuir*, 2005, **21**, 2923–2929.
38 C. B. Murray, C. R. Kagan and M. G. Bawendi, *Science*, 1995, **270**, 1335–1338.
39 N. R. Jana, *Angew. Chem., Int. Ed.*, 2004, **43**, 1536–1540.
40 S. A. Harfenist, Z. L. Wang, M. M. Alvarez, I. Vezmar and R. L. Whetten, *J. Phys. Chem.*, 1996, **100**, 13904–13910.
41 B. A. Grzybowski, A. Winkleman, J. A. Wiles, Y. Brumer and G. M. Whitesides, *Nat. Mater.*, 2003, **2**, 241–245.
42 E. C. Hao, B. Yang, J. H. Zhang, X. Zhang, J. Q. Sun and S. C. Shen, *J. Mater. Chem.*, 1998, **8**, 1327–1328.
43 J. Kolny, A. Kornowski and H. Weller, *Nano Lett.*, 2002, **2**, 361–364.
44 D. Lee, M. F. Rubner and R. E. Cohen, *Nano Lett.*, 2006, **6**, 2305–2312.
45 A. N. Shipway, M. Lahav, R. Gabai and I. Willner, *Langmuir*, 2000, **16**, 8789–8795.
46 D. A. Walker and V. K. Gupta, *Nanotechnology*, 2008, **19**.
47 R. Klajn, K. J. M. Bishop and B. A. Grzybowski, *Proc. Natl. Acad. Sci. U. S. A.*, 2007, **104**, 10305–10309.
48 Z. H. Sun, W. H. Ni, Z. Yang, X. S. Kou, L. Li and J. F. Wang, *Small*, 2008, **4**, 1287–1292.
49 D. Philp and J. F. Stoddart, *Angew. Chem., Int. Ed.*, 1996, **35**, 1155–1196.
50 C. A. Mirkin, R. L. Letsinger, R. C. Mucic and J. J. Storhoff, *Nature*, 1996, **382**, 607–609.
51 J. M. Lehn, *Angew. Chem., Int. Ed. Engl.*, 1990, **29**, 1304–1319.
52 M. Kimura, S. Kobayashi, T. Kuroda, K. Hanabusa and H. Shirai, *Adv. Mater.*, 2004, **16**, 335.
53 S. R. Johnson, S. D. Evans and R. Brydson, *Langmuir*, 1998, **14**, 6639–6647.
54 X. G. Hu, W. L. Cheng, T. Wang, E. K. Wang and S. J. Dong, *Nanotechnology*, 2005, **16**, 2164–2169.
55 L. Cusack, R. Rizza, A. Gorelov and D. Fitzmaurice, *Angew. Chem., Int. Ed. Engl.*, 1997, **36**, 848–851.
56 A. K. Boal, F. Ilhan, J. E. DeRouchey, T. Thurn-Albrecht, T. P. Russell and V. M. Rotello, *Nature*, 2000, **404**, 746–748.
57 A. P. Alivisatos, K. P. Johnsson, X. G. Peng, T. E. Wilson, C. J. Loweth, M. P. Bruchez and P. G. Schultz, *Nature*, 1996, **382**, 609–611.
58 Y. H. Wei, R. Klajn, A. O. Pinchuk and B. A. Grzybowski, *Small*, 2008, **4**, 1635–1639.
59 M. Golosovsky, Y. Saado and D. Davidov, *Appl. Phys. Lett.*, 1999, **75**, 4168–4170.
60 S. L. Tripp, S. V. Pusztay, A. E. Ribbe and A. Wei, *J. Am. Chem. Soc.*, 2002, **124**, 7914–7915.
61 H. Zeng, J. Li, J. P. Liu, Z. L. Wang and S. H. Sun, *Nature*, 2002, **420**, 395–398.
62 Y. Sahoo, M. Cheon, S. Wang, H. Luo, E. P. Furlani and P. N. Prasad, *J. Phys. Chem. B*, 2004, **108**, 3380–3383.
63 B. Kowalczyk, A. M. Kalsin, R. Orlik, K. J. M. Bishop, A. Z. Patashinskii, A. Mitus and B. A. Grzybowski, *Chem.–Eur. J.*, 2009, **15**, 2032–2035.
64 T. Hirakura, Y. Nomura, Y. Aoyama and K. Akiyoshi, *Biomacromolecules*, 2004, **5**, 1804–1809.
65 B. I. Ipe, S. Mahima and K. G. Thomas, *J. Am. Chem. Soc.*, 2003, **125**, 7174–7175.
66 N. Katsonis, M. Lubomska, M. M. Pollard, B. L. Feringa and P. Rudolf, *Prog. Surf. Sci.*, 2007, **82**, 407–434.
67 T. Vossmeyer, E. DeIonno and J. R. Heath, *Angew. Chem., Int. Ed. Engl.*, 1997, **36**, 1080–1083.
68 H. Hiramatsu and F. E. Osterloh, *Langmuir*, 2003, **19**, 7003–7011.
69 C. J. Orendorff, P. L. Hankins and C. J. Murphy, *Langmuir*, 2005, **21**, 2022–2026.
70 S. Cammas, K. Suzuki, C. Sone, Y. Sakurai, K. Kataoka and T. Okano, *J. Controlled Release*, 1997, **48**, 157–164.
71 N. N. Guan, J. Xu, L. Y. Wang and D. J. Sun, *Colloids Surf., A*, 2009, **346**, 221–228.
72 Y. Lu, G. L. Liu and L. P. Lee, *Nano Lett.*, 2005, **5**, 5–9.
73 E. C. M. Vermolen, A. Kuijk, L. C. Filion, M. Hermes, J. H. J. Thijssen, M. Dijkstra and A. van Blaaderen, *Proc. Natl. Acad. Sci. U. S. A.*, 2009, **106**, 16063–16067.
74 C. C. You, M. De, G. Han and V. M. Rotello, *J. Am. Chem. Soc.*, 2005, **127**, 12873–12881.
75 R. Hong, N. O. Fischer, A. Verma, C. M. Goodman, T. Emrick and V. M. Rotello, *J. Am. Chem. Soc.*, 2004, **126**, 739–743.
76 S. H. Brewer, W. R. Glomm, M. C. Johnson, M. K. Knag and S. Franzen, *Langmuir*, 2005, **21**, 9303–9307.
77 S. Phadtare, V. P. Vinod, K. Mukhopadhyay, A. Kumar, M. Rao, R. V. Chaudhari and M. Sastry, *Biotechnol. Bioeng.*, 2004, **85**, 629–637.
78 A. Gole, C. Dash, V. Ramakrishnan, S. R. Sainkar, A. B. Mandale, M. Rao and M. Sastry, *Langmuir*, 2001, **17**, 1674–1679.
79 P. Asuri, S. S. Karajanagi, A. A. Vertegel, J. S. Dordick and R. S. Kane, *J. Nanosci. Nanotechnol.*, 2007, **7**, 1675–1678.
80 Y. F. Huang, C. C. Huang and H. T. Chang, *Langmuir*, 2003, **19**, 7498–7502.
81 A. Gole, C. Dash, C. Soman, S. R. Sainkar, M. Rao and M. Sastry, *Bioconjugate Chem.*, 2001, **12**, 684–690.
82 A. Dyal, K. Loos, M. Noto, S. W. Chang, C. Spagnoli, K. Shafi, A. Ulman, M. Cowman and R. A. Gross, *J. Am. Chem. Soc.*, 2003, **125**, 1684–1685.
83 E. J. Bjerneld, Z. Foldes-Papp, M. Kall and R. Rigler, *J. Phys. Chem. B*, 2002, **106**, 1213–1218.
84 M. E. Aubin, D. G. Morales and K. Hamad-Schifferli, *Nano Lett.*, 2005, **5**, 519–522.
85 L. Wang and E. K. Wang, *Electrochem. Commun.*, 2004, **6**, 49–54.
86 T. Pascher, J. P. Chesick, J. R. Winkler and H. B. Gray, *Science*, 1996, **271**, 1558–1560.
87 H. Q. Liu, Y. Tian and Z. F. Deng, *Langmuir*, 2007, **23**, 9487–9494.
88 K. R. Brown, A. P. Fox and M. J. Natan, *J. Am. Chem. Soc.*, 1996, **118**, 1154–1157.
89 W. J. Parak, T. Pellegrino, C. M. Micheel, D. Gerion, S. C. Williams and A. P. Alivisatos, *Nano Lett.*, 2003, **3**, 33–36.
90 T. G. Drummond, M. G. Hill and J. K. Barton, *Nat. Biotechnol.*, 2003, **21**, 1192–1199.
91 C. M. Niemeyer, *Angew. Chem., Int. Ed.*, 2001, **40**, 4128–4158.
92 N. L. Rosi and C. A. Mirkin, *Chem. Rev.*, 2005, **105**, 1547–1562.
93 H. X. Li and L. Rothberg, *Proc. Natl. Acad. Sci. U. S. A.*, 2004, **101**, 14036–14039.
94 M. G. Warner and J. E. Hutchison, *Nat. Mater.*, 2003, **2**, 272–277.
95 J. L. Coffer, S. R. Bigham, X. Li, R. F. Pinizzotto, Y. G. Rho, R. M. Pirtle and I. L. Pirtle, *Appl. Phys. Lett.*, 1996, **69**, 3851–3853.
96 J. Wang, R. Polsky, A. Merkoci and K. L. Turner, *Langmuir*, 2003, **19**, 989–991.
97 M. Rycenga, J. M. McLellan and Y. Xia, *Adv. Mater.*, 2008, **20**, 2416.
98 J. Zhou, J. An, B. Tang, S. P. Xu, Y. X. Cao, B. Zhao, W. Q. Xu, J. J. Chang and J. R. Lombardi, *Langmuir*, 2008, **24**, 10407–10413.
99 D. A. Walker, C. E. Wilmer, B. Kowalczyk, K. J. M. Bishop and B. A. Grzybowski, *Nano Lett.*, 2010, **10**, 2275–2280.
100 P. E. Laibinis, G. M. Whitesides, D. L. Allara, Y. T. Tao, A. N. Parikh and R. G. Nuzzo, *J. Am. Chem. Soc.*, 1991, **113**, 7152–7167.
101 Y. N. Xia and G. M. Whitesides, *Annu. Rev. Mater. Sci.*, 1998, **28**, 153–184.
102 D. Witt, R. Klajn, P. Barski and B. A. Grzybowski, *Curr. Org. Chem.*, 2004, **8**, 1763–1797.
103 G. R. Maskaly, R. E. Garcia, W. C. Carter and Y. M. Chiang, *Phys. Rev. E: Stat., Nonlinear, Soft Matter Phys.*, 2006, **73**.
104 X. S. Shen, G. Z. Wang, X. Hong and W. Zhu, *CrystEngComm*, 2009, **11**, 753–755.
105 D. A. Walker, K. P. Browne, B. Kowalczyk and B. A. Grzybowski, *Angew. Chem., Int. Ed.*, 2010, **49**, 6760–6763.
106 C. M. Goodman, C. D. McCusker, T. Yilmaz and V. M. Rotello, *Bioconjugate Chem.*, 2004, **15**, 897–900.
107 T. R. Pisanic, J. D. Blackwell, V. I. Shubayev, R. R. Finones and S. Jin, *Biomaterials*, 2007, **28**, 2572–2581.
108 P. K. Stoimenov, R. L. Klinger, G. L. Marchin and K. J. Klabunde, *Langmuir*, 2002, **18**, 6679–6686.
109 T. H. Chung, S. H. Wu, M. Yao, C. W. Lu, Y. S. Lin, Y. Hung, C. Y. Mou, Y. C. Chen and D. M. Huang, *Biomaterials*, 2007, **28**, 2959–2966.
110 S. Patil, A. Sandberg, E. Heckert, W. Self and S. Seal, *Biomaterials*, 2007, **28**, 4600–4607.
111 C. Wilhelm and F. Gazeau, *Biomaterials*, 2008, **29**, 3161–3174.
112 R. G. Nuzzo and D. L. Allara, *J. Am. Chem. Soc.*, 1983, **105**, 4481–4483.
113 D. L. Allara and R. G. Nuzzo, *Langmuir*, 1985, **1**, 45–52.
114 R. Heinz and J. P. Rabe, *Langmuir*, 1995, **11**, 506–511.

115 A. Dhirani, M. A. Hines, A. J. Fisher, O. Ismail and P. Guyotsionnest, *Langmuir*, 1995, **11**, 2609–2614.
116 A. Nemetz, T. Fischer, A. Ulman and W. Knoll, *J. Chem. Phys.*, 1993, **98**, 5912–5919.
117 S. M. Driver and D. P. Woodruff, *Langmuir*, 2000, **16**, 6693–6700.
118 O. Azzaroni, M. E. Vela, M. Fonticelli, G. Benitez, P. Carro, B. Blum and R. C. Salvarezza, *J. Phys. Chem. B*, 2003, **107**, 13446–13454.
119 A. Imanishi, K. Isawa, F. Matsui, T. Tsuduki, T. Yokoyama, H. Kondoh, Y. Kitajima and T. Ohta, *Surf. Sci.*, 1998, **407**, 282–292.
120 H. Rieley, G. K. Kendall, A. Chan, R. G. Jones, J. Ludecke, D. P. Woodruff and B. C. C. Cowie, *Surf. Sci.*, 1997, **392**, 143–152.
121 J. A. Williams and C. B. Gorman, *J. Phys. Chem. C*, 2007, **111**, 12804–12810.
122 J. C. Love, D. B. Wolfe, R. Haasch, M. L. Chabinyc, K. E. Paul, G. M. Whitesides and R. G. Nuzzo, *J. Am. Chem. Soc.*, 2003, **125**, 2597–2609.
123 A. Carvalho, M. Geissler, H. Schmid, B. Michel and E. Delamarche, *Langmuir*, 2002, **18**, 2406–2412.
124 H. Murayama, N. Ichikuni, Y. Negishi, T. Nagata and T. Tsukuda, *Chem. Phys. Lett.*, 2003, **376**, 26–32.
125 Z. Mekhalif, J. Riga, J. J. Pireaux and J. Delhalle, *Langmuir*, 1997, **13**, 2285–2290.
126 S. Noel, F. Houze, L. Boyer, Z. Mekhalif, J. Delhalle and R. Caudano, *IEEE Trans. Compon. Packag. Technol.*, 1999, **22**, 79–84.
127 M. E. Castro and J. M. White, *Surf. Sci.*, 1991, **257**, 22–32.
128 E. Ruckenstein and Z. F. Li, *Adv. Colloid Interface Sci.*, 2005, **113**, 43–63.
129 D. D. Gandhi, M. Lane, Y. Zhou, A. P. Singh, S. Nayak, U. Tisch, M. Eizenberg and G. Ramanath, *Nature*, 2007, **447**, 299–U292.
130 Y. G. Cai, *Langmuir*, 2009, **25**, 5594–5601.
131 A. R. Morrill, D. T. Duong, S. J. Lee and M. Moskovits, *Chem. Phys. Lett.*, 2009, **473**, 116–119.
132 R. Helmy and A. Y. Fadeev, *Langmuir*, 2002, **18**, 8924–8928.
133 K. Shafi, A. Ulman, X. Z. Yan, N. L. Yang, M. Himmelhaus and M. Grunze, *Langmuir*, 2001, **17**, 1726–1730.
134 M. A. White, J. A. Johnson, J. T. Koberstein and N. J. Turro, *J. Am. Chem. Soc.*, 2006, **128**, 11356–11357.
135 C. Yee, G. Kataby, A. Ulman, T. Prozorov, H. White, A. King, M. Rafailovich, J. Sokolov and A. Gedanken, *Langmuir*, 1999, **15**, 7111–7115.
136 A. K. Gupta and M. Gupta, *Biomaterials*, 2005, **26**, 3995–4021.
137 Y. Sahoo, H. Pizem, T. Fried, D. Golodnitsky, L. Burstein, C. N. Sukenik and G. Markovich, *Langmuir*, 2001, **17**, 7907–7911.
138 F. Schreiber, *Prog. Surf. Sci.*, 2000, **65**, 151–256.
139 M. J. Hostetler, J. E. Wingate, C. J. Zhong, J. E. Harris, R. W. Vachet, M. R. Clark, J. D. Londono, S. J. Green, J. J. Stokes, G. D. Wignall, G. L. Glish, M. D. Porter, N. D. Evans and R. W. Murray, *Langmuir*, 1998, **14**, 17–30.
140 C. Haensch, S. Hoeppener and U. S. Schubert, *Chem. Soc. Rev.*, 2010, **39**, 2323–2334.
141 R. K. Smith, P. A. Lewis and P. S. Weiss, *Prog. Surf. Sci.*, 2004, **75**, 1–68.
142 J. J. Gooding, F. Mearns, W. R. Yang and J. Q. Liu, *Electroanalysis*, 2003, **15**, 81–96.
143 M. O. de la Cruz, *Soft Matter*, 2008, **4**, 1735–1739.
144 H. Helmholtz, *Proggendorff's Annals*, 1853, **89**, 211–233, 353–377.
145 G. Gouy, *J. Phys.*, 1910, **4**, 457.
146 G. Gouy, *Comt. Rend.*, 1909, **149**, 654.
147 D. L. Chapman, *Phil. Mag.*, 1913, **6**, 475.
148 D. R. Lide, ed., *CRC Handbook of Chemistry and Physics*, CRC Press, New York, 2005.
149 K. Sharp, A. Jeancharles and B. Honig, *J. Phys. Chem.*, 1992, **96**, 3822–3828.
150 R. Messina, *J. Chem. Phys.*, 2002, **117**, 11062–11074.
151 G. I. Guerrero-Garcia, E. Gonzalez-Tovar and M. O. de la Cruz, *Soft Matter*, 2010, **6**, 2056–2065.
152 R. Ramirez and R. Kjellander, *J. Chem. Phys.*, 2003, **119**, 11380–11395.
153 P. Gonzalez-Mozuelos, M. S. Yeom and M. O. de la Cruz, *Eur. Phys. J. E*, 2005, **16**, 167–178.
154 G. I. Guerrero-Garcia, E. Gonzalez-Tovar, M. Lozada-Cassou and F. D. Guevara-Rodriguez, *J. Chem. Phys.*, 2005, **123**.
155 G. I. Guerrero-Garcia, E. Gonzalez-Tovar and M. Chavez-Paez, *Phys. Rev. E: Stat., Nonlinear, Soft Matter Phys.*, 2009, **80**.
156 F. Jimenez-Angeles and M. Lozoda-Cassou, *J. Phys. Chem. B*, 2004, **108**, 7286–7296.
157 M. Quesada-Perez, E. Gonzalez-Tovar, A. Martin-Molina, M. Lozada-Cassou and R. Hidalgo-Alvarez, *ChemPhysChem*, 2003, **4**, 234–248.
158 G. I. Guerrero-Garcia, E. Gonzalez-Tovar, M. Chavez-Paez and M. Lozada-Cassou, *J. Chem. Phys.*, 2010, **132**.
159 A. P. dos Santos, A. Diehl and Y. Levin, *J. Chem. Phys.*, 2010, **132**.
160 A. G. Moreira and R. R. Netz, *Phys. Rev. Lett.*, 2001, **87**.
161 A. Naji, S. Jungblut, A. G. Moreira and R. R. Netz, *Phys. A*, 2005, **352**, 131–170.
162 J. W. Zwanikken and M. O. de la Cruz, *Phys. Rev. E: Stat., Nonlinear, Soft Matter Phys.*, 2010, **82**, 050401.
163 This value can also be computed for dipoles and higher order multipoles from changes in the electric field and its derivatives.
164 O. Stern, *Zeitschrift fur Elektrochemie*, 1924, **30**, 508–516.
165 A. Travesset and S. Vangaveti, *J. Chem. Phys.*, 2009, **131**.
166 H. Trauble and H. Eibl, *Proc. Natl. Acad. Sci. U. S. A.*, 1974, **71**, 214–219.
167 D. Y. C. Chan and D. J. Mitchell, *J. Colloid Interface Sci.*, 1983, **95**, 193–197.
168 A. Coskun, P. J. Wesson, R. Klajn, A. Trabolsi, L. Fang, M. A. Olson, S. K. Dey, B. A. Grzybowski and J. F. Stoddart, *J. Am. Chem. Soc.*, 2010, **132**, 4310–4320.
169 K. J. M. Bishop, C. E. Wilmer, S. Soh and B. A. Grzybowski, *Small*, 2009, **5**, 1600–1630.
170 J. T. G. Overbeek, *Colloids Surf.*, 1990, **51**, 61–75.
171 B. V. Derjaguin, *Kolloid-Z.*, 1934, **69**, 155.
172 B. V. Derjaguin, *Acta Physico Chimica U.S.S.R.*, 1939, **10**, 333.
173 R. Hogg, T. W. Healy and D. W. Fuerstenau, *Trans. Faraday Soc.*, 1966, **62**, 1638.
174 A. B. Glendinning and W. B. Russel, *J. Colloid Interface Sci.*, 1983, **93**, 95–104.
175 J. W. Krozel and D. A. Saville, *J. Colloid Interface Sci.*, 1992, **150**, 365–373.
176 S. L. Carnie, D. Y. C. Chan and J. Stankovich, *J. Colloid Interface Sci.*, 1994, **165**, 116–128.
177 S. L. Carnie, D. Y. C. Chan and J. S. Gunning, *Langmuir*, 1994, **10**, 2993–3009.
178 E. J. W. Verwey and J. T. G. Overbeek, *Theory of the Stability of Lyophobic Colloids*, Elsevier, New York, 1948.
179 J. C. F. Toledano, F. Sciortino and E. Zaccarelli, *Soft Matter*, 2009, **5**, 2390–2398.
180 E. Sanz, K. A. White, P. S. Clegg and M. E. Cates, *Phys. Rev. Lett.*, 2009, **103**.
181 M. Brunner, J. Dobnikar, H.-H. von Grunberg and C. Bechinger, *Phys. Rev. Lett.*, 2004, **92**, 078301.
182 J. Dobnikar, M. Brunner, H. H. von Grunberg and C. Bechinger, *Phys. Rev. E: Stat., Nonlinear, Soft Matter Phys.*, 2004, **69**.
183 J. W. Merrill, S. K. Sainis and E. R. Dufresne, *Phys. Rev. Lett.*, 2009, **103**, 138301.
184 B. V. R. Tata, M. Rajalakshmi and A. K. Arora, *Phys. Rev. Lett.*, 1992, **69**, 3778–3781.
185 C. Russ, H. H. von Grunberg, M. Dijkstra and R. van Roij, *Phys. Rev. E: Stat. Phys., Plasmas, Fluids, Relat. Interdiscip. Top.*, 2002, **66**.
186 A. P. Hynninen, M. Dijkstra and R. van Roij, *Phys. Rev. E: Stat., Nonlinear, Soft Matter Phys.*, 2004, **69**.
187 J. Dobnikar, Y. Chen, R. Rzehak and H. H. von Grunberg, *J. Phys.: Condens. Matter*, 2003, **15**, S263–S268.
188 G. Vernizzi and M. O. de la Cruz, *Proc. Natl. Acad. Sci. U. S. A.*, 2007, **104**, 18382–18386.
189 M. J. Stevens, *J. Chem. Phys.*, 2004, **121**, 11942–11948.
190 K. J. M. Bishop and B. A. Grzybowski, *ChemPhysChem*, 2007, **8**, 2171–2176.
191 A. Albert and E. P. Serjeant, *Ionization Constants of Acids and Bases*, Methuen & Co Ltd., London, 1962.
192 M. Tagliazucchi, M. O. de la Cruz and I. Szleifer, *Proc. Natl. Acad. Sci. U. S. A.*, 2010, **107**, 5300–5305.
193 P. Gong, J. Genzer and I. Szleifer, *Physical Review Letters*, 2007, **98**.
194 M. A. Carignano and I. Szleifer, *J. Chem. Phys.*, 1993, **98**, 5006–5018.
195 R. Klajn, L. Fang, A. Coskun, M. A. Olson, P. J. Wesson, J. F. Stoddart and B. A. Grzybowski, *J. Am. Chem. Soc.*, 2009, **131**, 4233.

196 P. D. Yates, G. V. Franks, S. Biggs and G. J. Jameson, *Colloids Surf., A*, 2005, **255**, 85–90.
197 A. Y. Kim and J. C. Berg, *J. Colloid Interface Sci.*, 2000, **229**, 607–614.
198 J. M. Lopez-Lopez, A. Schmitt, A. Moncho-Jorda and R. Hidalgo-Alvarez, *Soft Matter*, 2006, **2**, 1025–1042.
199 A. O. Pinchuk, A. M. Kalsin, B. Kowalczyk, G. C. Schatz and B. A. Grzybowski, *J. Phys. Chem. C*, 2007, **111**, 11816–11822.
200 S. K. Smoukov, K. J. M. Bishop, B. Kowalczyk, A. M. Kalsin and B. A. Grzybowski, *J. Am. Chem. Soc.*, 2007, **129**, 15623–15630.
201 A. M. Kalsin, A. O. Pinchuk, S. K. Smoukov, M. Paszewski, G. C. Schatz and B. A. Grzybowski, *Nano Lett.*, 2006, **6**, 1896–1903.
202 A. M. Kalsin, B. Kowalczyk, P. Wesson, M. Paszewski and B. A. Grzybowski, *J. Am. Chem. Soc.*, 2007, **129**, 6664.
203 A. M. Kalsin, B. Kowalczyk, S. K. Smoukov, R. Klajn and B. A. Grzybowski, *J. Am. Chem. Soc.*, 2006, **128**, 15046–15047.
204 H. Sellers, A. Ulman, Y. Shnidman and J. E. Eilers, *J. Am. Chem. Soc.*, 1993, **115**, 9389–9401.
205 B. A. Grzybowski, *Chemistry in Motion: Reaction-Diffusion Systems for Micro- and Nanotechnology*, John Wiley & Sons Ltd., West Sussex, UK, 2009.
206 Z. Y. Tang, N. A. Kotov and M. Giersig, *Science*, 2002, **297**, 237–240.
207 Z. L. Zhang, Z. Y. Tang, N. A. Kotov and S. C. Glotzer, *Nano Lett.*, 2007, **7**, 1670–1675.
208 S. M. Liff, N. Kumar and G. H. McKinley, *Nat. Mater.*, 2007, **6**, 76–83.
209 M. Es-Souni and H. Fischer-Brandies, *Adv. Funct. Mater.*, 2008, **18**, 3179–3188.
210 S. Huda, S. K. Smoukov, H. Nakanishi, B. Kowalczyk, K. Bishop and B. A. Grzybowski, *ACS Appl. Mater. Interfaces*, 2010, **2**, 1206–1210.
211 K. V. Tretiakov, K. J. M. Bishop, B. Kowalczyk, A. Jaiswal, M. A. Poggi and B. A. Grzybowski, *J. Phys. Chem. A*, 2009, **113**, 3799–3803.
212 M. G. Song, K. J. M. Bishop, A. O. Pinchuk, B. Kowalczyk and B. A. Grzybowski, *J. Phys. Chem. C*, 2010, **114**, 8800–8805.
213 L. Filion, M. Marechal, B. van Oorschot, D. Pelt, F. Smallenburg and M. Dijkstra, *Physical Review Letters*, 2009, **103**.
214 V. Sharma, Q. F. Yan, C. C. Wong, W. C. Cartera and Y. M. Chiang, *J. Colloid Interface Sci.*, 2009, **333**, 230–236.
215 T. Ming, X. S. Kou, H. J. Chen, T. Wang, H. L. Tam, K. W. Cheah, J. Y. Chen and J. F. Wang, *Angew. Chem., Int. Ed.*, 2008, **47**, 9685–9690.
216 F. Huang, R. Rotstein, S. Fraden, K. E. Kasza and N. T. Flynn, *Soft Matter*, 2009, **5**, 2766–2771.
217 A. Guerrero-Martinez, J. Perez-Juste, E. Carbo-Argibay, G. Tardajos and L. M. Liz-Marzan, *Angew. Chem., Int. Ed.*, 2009, **48**, 9484–9488.
218 S. C. Glotzer and M. J. Solomon, *Nat. Mater.*, 2007, **6**, 557–562.
219 R. Boyack and E. C. Le Ru, *Phys. Chem. Chem. Phys.*, 2009, **11**, 7398–7405.
220 S. B. Chaney, S. Shanmukh, R. A. Dluhy and Y. P. Zhao, *Appl. Phys. Lett.*, 2005, **87**, 3.
221 E. Hao and G. C. Schatz, *J. Chem. Phys.*, 2004, **120**, 357–366.
222 S. M. Nie and S. R. Emery, *Science*, 1997, **275**, 1102–1106.
223 B. Nikoobakht, J. P. Wang and M. A. El-Sayed, *Chem. Phys. Lett.*, 2002, **366**, 17–23.
224 G. B. Irani, T. Huen and F. Wooten, *J. Opt. Soc. Am.*, 1971, **61**, 128.
225 R. J. Hunter, *Foundations of Colloid Science*, Oxford University Press, New York, 2001.
226 Our estimates of electrostatic energies neglect edge effects due to finite sizes of the triangles. We note, however, that because of screening, electrostatic forces are relatively-short ranged (∼5 nm), the edge effects are negligible (at most ∼12% of the total electrostatic energy).
227 Charge density was calculated from the electrophoretic mobility, as determined by a Malvern Zetasizer Nano-ZS.
228 B. Kowalczyk, D. A. Walker, S. Soh and B. A. Grzybowski, *Angew. Chem., Int. Ed.*, 2010, **49**, 5737–5741.
229 M. C. Roco, in *Handbook on Nanoscience, Engineering and Technology*, Taylor and Francis, 2 edn, 2007, pp. 3.1-3.26.
230 D. Derks, H. Wisman, A. van Blaaderen and A. Imhof, *J. Phys.: Condens. Matter*, 2004, **16**, S3917–S3927.
231 A. Yethiraj and A. van Blaaderen, *Nature*, 2003, **421**, 513–517.
232 U. Gasser, E. R. Weeks, A. Schofield, P. N. Pusey and D. A. Weitz, *Science*, 2001, **292**, 258–262.
233 E. H. A. de Hoog, W. K. Kegel, A. van Blaaderen and H. N. W. Lekkerkerker, *Phys. Rev. E: Stat. Phys., Plasmas, Fluids, Relat. Interdiscip. Top.*, 2001, **64**.
234 J. P. Hoogenboom, D. L. J. Vossen, C. Faivre-Moskalenko, M. Dogterom and A. van Blaaderen, *Appl. Phys. Lett.*, 2002, **80**, 4828–4830.
235 M. E. Leunissen, H. R. Vutukuri and A. van Blaaderen, *Adv. Mater.*, 2009, **21**, 3116.
236 A. van der Horst, A. I. Campbell, L. K. van Vugt, D. A. M. Vanmaekelbergh, M. Dogterom and A. van Blaaderen, *Opt. Express*, 2007, **15**, 11629–11639.
237 C.-W. Li and B. E. Volcani, *Philos. Trans. R. Soc. London, Ser. B*, 1984, **304**, 519–528.
238 K. Y. Win and S. S. Feng, *Biomaterials*, 2005, **26**, 2713–2722.
239 B. Honig and A. Nicholls, *Science*, 1995, **268**, 1144–1149.
240 G. S. Lee, Y. J. Lee and K. B. Yoon, *J. Am. Chem. Soc.*, 2001, **123**, 9769–9779.
241 R. C. Mucic, J. J. Storhoff, C. A. Mirkin and R. L. Letsinger, *J. Am. Chem. Soc.*, 1998, **120**, 12674–12675.
242 E. Dujardin, L. B. Hsin, C. R. C. Wang and S. Mann, *Chem. Commun.*, 2001, 1264–1265.
243 C. Chen, M. C. Daniel, Z. T. Quinkert, M. De, B. Stein, V. D. Bowman, P. R. Chipman, V. M. Rotello, C. C. Kao and B. Dragnea, *Nano Lett.*, 2006, **6**, 611–615.
244 H. Ohshima and A. Hyono, *J. Colloid Interface Sci.*, 2009, **333**, 202–208.
245 H. C. Hamaker, *Physics*, 1937, **4**, 1058.
246 J. Mahanty and B. W. Ninham, *Dispersion Forces*, Academic Press, London, 1976.
247 L. R. White, J. N. Israelachvili and B. W. Ninham, *J. Chem. Soc., Faraday Trans. 1*, 1976, **72**, 2526–2536.
248 D. Wang, R. J. Nap, I. Lagzi, B. Kowalczyk, S. Han, I. Szleifer and B. A. Grzybowski, *J. Am. Chem. Soc.*, 2011, DOI: 10.1021/ja108154a.
249 A. M. Kalsin and B. A. Grzybowski, *Nano Lett.*, 2007, **7**, 1018–1021.

